On the Behavior of Ocean Analysis and Forecast Error Covariance in the Presence of Baroclinic Instability

by

Andrew M. Moore[a*] and Hernan G. Arango[b]

a: Department of Ocean Sciences, University of California Santa Cruz
1156 High Street, Santa Cruz CA 95062, U.S.A.
b: Department of Marine and Coastal Sciences, Rutgers, The State University of New Jersey,
71 Dudley Road, New Brunswick NJ 08901, U.S.A.

* Corresponding author: ammoore@ucsc.edu
Department of Ocean Sciences, University of California, 1156 High Street,
Santa Cruz CA 95062

Abstract

The properties of the expected analysis and forecast error covariance matrices are explored using a novel method based on the tangent linearization and adjoint of a 4-dimensional variational (4D-Var) data assimilation system. The method is applied to the mesoscale circulation that develops in the presence of a baroclinically unstable mid-latitude ocean temperature front using a series of paternal twin experiments that employ both strong and weak constraint 4D-Var. Adopting the traditional view of Empirical Orthogonal Functions (EOFs) of a covariance matrix as the semi-major axes of a multi-dimensional hyper-ellipsoid, variations in the volume of the analysis and forecast error hyper-ellipsoids are explored which provides information about the flow of probability through state-space. The complementary variations in the expected total variance of the covariance matrix are also investigated. Two different kinds of behavior are identified that are associated with either the demise or growth of baroclinic instabilities. In both cases, the volume of the hyper-ellipsoid decreases during the 4D-Var analysis cycle. During the subsequent forecasts, the volume of the forecast error hyper-ellipsoid initially continues to collapse under both scenarios. During this time, the hyper-ellipsoid becomes increasingly elongated along some of the semi-major axes as forecast errors grow in preferential directions. Growth in these directions is controlled by the most unstable error modes, and projection of forecast error on to the precursors of these modes has been shown previously to be characterized by upscale energy transfer and non-normal processes. For the case of the growing wave, the forecast error hyper-ellipsoid continues to collapse through to the end of the forecast period. However, for the decaying wave, the hyper-ellipsoid may undergo expansion at longer forecast lead times.

Keywords: 4D-Var; error covariance; adjoint methods; baroclinic instability

1. Introduction

An important element of operational analysis and forecast systems for the ocean and atmosphere is the quantification of the errors and uncertainties in the resulting circulation estimates. Since many operational systems these days are based on an ensemble approach, analysis and forecast ensembles provide a convenient means for estimating error covariance properties. Such approximations, however, are of reduced rank in nature, and generally, underestimate the actual errors. For example, some form of covariance inflation is typically required in ensemble Kalman filters due to the limited number of members that are used (*e.g.*, Anderson, 2007). In addition, localization is necessary to ameliorate spurious correlations (and rank-deficiency) due to the limited ensemble size (Gaspari and Cohn, 1999). In variational data assimilation systems, covariance information is difficult to compute (Ngodock *et al.*, 2020) but can be estimated from an approximation of the Kalman gain matrix, although it is typically an underestimate of the actual error covariance (Fisher and Courtier, 1995).

The very large dimension of most geophysical problems of interest precludes the explicit computation of analysis and forecast error covariance matrices. However, many important properties of these covariances can be computed if it is possible to compute the product of the matrix with a vector. In this paper, we explore an alternative approach for computing the expected analysis and forecast error covariance, which makes direct use of the tangent linear and adjoint of a 4-dimensional variational (4D-Var) data assimilation system to compute a matrix-vector product. It should be stated at the outset that the approach used here is extraordinarily demanding computationally and is not suitable for a large operational analysis-forecast system. However, as we will demonstrate, our approach is of theoretical and mathematical interest because it has the desirable property of providing an explicit operator for the analysis and forecast error covariance, which makes it very appealing. Despite the heavy computational burden in a conventional 4D-Var system, recent developments in 4D-Var promise very substantial reductions in the computational cost (Fisher *et* al., 2011; D'Amore *et al.,* 2014; Arcucci *et al.,* 2015; Fisher and Gürol, 2017) which could make the approach adopted here more tractable in large models in the future.

In light of the computationally heavy burden, attention is restricted to an exploration of the properties of analysis and forecast error covariance in a small, but very relevant, computational domain. Specifically, we will consider the expected covariance properties of errors that develop in the ocean mesoscale circulation environment that results from the adjustment of a baroclinically unstable temperature front at mid-latitudes. Fronts are a common feature of the ocean circulation, so the results presented here are of broad interest and generally applicable in many situations. For example, analysis and prediction of oceanic fronts and their incumbent eddies in coastal ocean environments is an important mandate of many operational forecasting centers because of the significant role that these circulation features play in controlling local air-sea interactions, the health of marine ecosystems, and ocean acidification events. Therefore, the results presented here have some potentially very practical applications.

A description of the mathematical formulation of the analysis and forecast error covariance in terms of the tangent linearization of the entire data assimilation system is presented in section 2, while section 3 describes the experimental set-up used to explore the utility of the method introduced in section 2. The properties of the expected analysis and forecast errors for a frontal system are presented in sections 4 and 5. Section 6 demonstrates the connection between the method used here and the closely related study of Smith *et al.* (2015). A summary and conclusions follow in section 7.

2. Methodology

The approach developed for estimating the expected analysis and forecast error covariance is based on the work of Moore *et al.* (2012) (hereafter MAB) using a 4D-Var approach. For this reason, the following discussion is focused on 4D-Var, but the same methodology could, in principle, be applied to any linearized data assimilation algorithm.

a. The expected analysis error covariance

A standard notation will be adopted here (Ide *et al.,* 1997), where $\boldsymbol{x}$ represents the state-vector of the system under consideration, while $\boldsymbol{x}^b$ and $\boldsymbol{x}^a$ denote the background and analysis estimates of $\boldsymbol{x}$ respectively. For any linear data assimilation system, the best, linear, unbiased estimate (BLUE; aka *analysis*) can be expressed as:

$$\boldsymbol{x}^a = \boldsymbol{x}^b + \boldsymbol{K}\left(\boldsymbol{y}^o - H(\boldsymbol{x}^b)\right) \qquad (1)$$

where $\boldsymbol{y}^o$ is the vector of observations, and H is the observation operator that maps $\boldsymbol{x}^b$ to the space-time location of each datum. The matrix $\boldsymbol{K}$ is the Kalman gain, and can be expressed as:

$$\boldsymbol{K} = \boldsymbol{B}\boldsymbol{H}^T(\boldsymbol{H}\boldsymbol{B}\boldsymbol{H}^T + \boldsymbol{R})^{-1} \qquad (2)$$

where $\boldsymbol{B}$ and $\boldsymbol{R}$ are the background and observation error covariance matrices, respectively, and $\boldsymbol{H}$ is the linearized observation operator. In the case of 4D-Var, data are assimilated over a window in time and H also includes the nonlinear model, while $\boldsymbol{H}$ represents the tangent linear model sampled at the observation points. The adjoint model forced at the observation points is represented by $\boldsymbol{H}^T$. In the case of strong constraint 4D-Var, $\boldsymbol{B} = \boldsymbol{B}_{\boldsymbol{x}}$ and describes the statistics of the errors in the initial conditions. For the weak constraint case, errors in the model are also accounted for by augmenting the background error covariance matrix so that $\boldsymbol{B} = diag(\boldsymbol{B}_{\boldsymbol{x}}, \boldsymbol{Q})$ where $\boldsymbol{Q}$ is the model error covariance matrix. A schematic of a typical analysis-forecast cycle for both flavors of 4D-Var is shown in Fig. 1, where the interval $t = [-\tau, 0]$ denotes the analysis window, and $t = (0, t]$ represents the forecast interval. The analysis given by (1) is valid at the beginning of the analysis window and must be integrated forward in time to $t = 0$ in order to make a forecast. Based on (1) and (2), the covariance of the expected errors in the analysis $\boldsymbol{x}^a$ can be written as:

$$\boldsymbol{A}(-\tau) = (\boldsymbol{I} - \boldsymbol{K}\boldsymbol{H})\boldsymbol{B}(\boldsymbol{I} - \boldsymbol{K}\boldsymbol{H})^T + \boldsymbol{K}\boldsymbol{R}\boldsymbol{K}^T \qquad (3)$$

(Daley, 1991). As in (1), this estimate of $\boldsymbol{A}$ is valid at time $t = -\tau$.

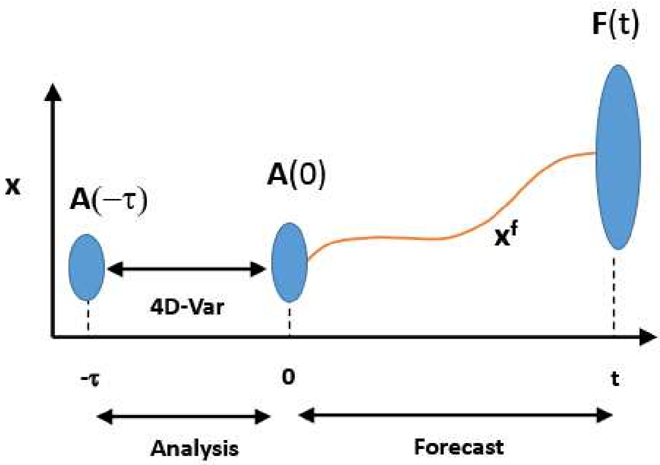

Figure 1: A schematic showing a typical analysis and forecast cycle that employs 4D-Var data assimilation. The analysis cycle spans the time interval $[-\tau, 0]$ while the forecast cycle spans the interval $(0, t]$. The expected errors in the analyses at the forecast start time $t = 0$ are described by the analysis error covariance matrix $\boldsymbol{A}(0)$, while the expected errors in the forecast $\boldsymbol{x}^f$ are represented by the forecast error covariance matrix $\boldsymbol{F}(t)$.

The goal of 4D-Var is to identify the analysis $\boldsymbol{x}^a(-\tau)$ that minimizes a cost function that is a quadratic measure of the weighted departures of $\boldsymbol{x}$ from the background and the observations. Because the resulting minimization problem is nonlinear, it is common practice to apply the incremental approach of Courtier *et al.* (1994), where the estimation procedure is linearized about the background $\boldsymbol{x}^b$ over the interval $t = [-\tau, 0]$. The resulting algorithm is equivalent to a Gauss-Newton method (Lawless *et al.*, 2005) and comprises so-called inner-loops and outer-loops. The minimization of the non-quadratic cost function proceeds via a sequence of linear minimization problems where the latter is accomplished during the inner-loop iterations and identifies an increment $\delta\boldsymbol{x}(-\tau)$ to $\boldsymbol{x}^b(-\tau)$. Following the completion of a sequence of inner-loops, the state vector estimate $\boldsymbol{x}(-\tau)$ is updated using the most recent increment during an outer-loop, and another linear minimization problem is solved via a new set of inner-loops. After n outer-loops, the analysis is given by:

$$\boldsymbol{x}^a = \boldsymbol{x}^b + \sum_{i=1}^{n} \delta\boldsymbol{x}_i, \tag{4}$$

and the expected analysis error covariance matrix is given by:

$$\begin{aligned}\boldsymbol{A}_n(-\tau) = &\left[\prod_{i=n}^{1}(\boldsymbol{I} - \boldsymbol{K}_i\boldsymbol{H}_{i-1})\right]\boldsymbol{B}\left[\prod_{i=n}^{1}(\boldsymbol{I} - \boldsymbol{K}_i\boldsymbol{H}_{i-1})\right]^T \\ &+ \left[\sum_{j=1}^{n-1}\prod_{i=n}^{j+1}(\boldsymbol{I} - \boldsymbol{K}_i\boldsymbol{H}_{i-1})\boldsymbol{K}_j + \boldsymbol{K}_n\right]\boldsymbol{R}\left[\sum_{j=1}^{n-1}\prod_{i=n}^{j+1}(\boldsymbol{I} - \boldsymbol{K}_i\boldsymbol{H}_{i-1})\boldsymbol{K}_j + \boldsymbol{K}_n\right]^T\end{aligned} \tag{5}$$

where $\boldsymbol{K}_i$ is the Kalman gain resulting from outer-loop i and $\boldsymbol{H}_{i-1}$ is the tangent linear observation operator linearized about $\boldsymbol{x}_{i-1}$. During the first outer-loop $\boldsymbol{H}_0 \equiv \boldsymbol{H}_b$, which is the observation operator linearized about $\boldsymbol{x}^b$.

b. Analysis error covariances from the tangent linearization of 4D-Var

Belo-Pereira and Berre (2006) and Berre *et al.* (2006) have demonstrated that estimates of the expected analysis error covariance matrix can be computed by perturbing an analysis $\boldsymbol{x}^a$ to create an analysis ensemble. Each member of the analysis ensemble is generated by rerunning the data assimilation system using a perturbed background and perturbed observations. The perturbations are drawn from normal distributions with zero mean and error covariances $\boldsymbol{B}$ and $\boldsymbol{R}$, respectively. As shown by these authors, the covariance of the resulting analysis ensemble mimics the covariance of the expected uncertainties in the unperturbed analysis $\boldsymbol{x}^a$. In the case of 4D-Var, this would be an estimate of $\boldsymbol{A}_n(-\tau)$ in Fig. 1, and the original unperturbed analysis $\boldsymbol{x}^a$ represents the ensemble mean.

By extending these ideas, MAB showed that as the size of the analysis ensemble approaches infinity, the ensemble covariance can be expressed in terms of a tangent linearization of the data assimilation system and its adjoint. In the context of the present work, this would be the tangent linearization of the entire 4D-Var algorithm and the corresponding adjoint. Specifically, any linear data assimilation system that solves for the BLUE in (1) can be generalized so that:

$$\boldsymbol{x}^a = \boldsymbol{x}^b + \mathcal{K}(\boldsymbol{d}) \tag{6}$$

where $\boldsymbol{d} = \left(\boldsymbol{y}^o - H(\boldsymbol{x}^b)\right)$ represents the innovation vector, and $\mathcal{K}(\boldsymbol{d})$ denotes the data assimilation algorithm, which, in general, will be a nonlinear function of $\boldsymbol{d}$. For example, 4D-Var proceeds by minimizing the cost function using a conjugate gradient method, an inherently nonlinear procedure based on $\boldsymbol{d}$. Using (6) and following MAB, equation (5) can be re-expressed as:

$$\begin{aligned}\boldsymbol{A}_n(-\tau) = &\left[\prod_{i=n}^{1}\left(\boldsymbol{I} - \frac{\partial\mathcal{K}}{\partial\boldsymbol{d}_i}\boldsymbol{H}_{i-1}\right)\right]\boldsymbol{B}\left[\prod_{i=n}^{1}\left(\boldsymbol{I} - \frac{\partial\mathcal{K}}{\partial\boldsymbol{d}_i}\boldsymbol{H}_{i-1}\right)\right]^T \\ &+ \left[\sum_{j=1}^{n-1}\prod_{i=n}^{j+1}\left(\boldsymbol{I} - \frac{\partial\mathcal{K}}{\partial\boldsymbol{d}_i}\boldsymbol{H}_{i-1}\right)\frac{\partial\mathcal{K}}{\partial\boldsymbol{d}_j} \right. \\ &\left. + \frac{\partial\mathcal{K}}{\partial\boldsymbol{d}_n}\right]\boldsymbol{R}\left[\sum_{j=1}^{n-1}\prod_{i=n}^{j+1}\left(\boldsymbol{I} - \frac{\partial\mathcal{K}}{\partial\boldsymbol{d}_i}\boldsymbol{H}_{i-1}\right)\frac{\partial\mathcal{K}}{\partial\boldsymbol{d}_j} + \frac{\partial\mathcal{K}}{\partial\boldsymbol{d}_n}\right]^T\end{aligned} \tag{7}$$

where $\boldsymbol{d}_i = \left(\boldsymbol{y}^o - H(\boldsymbol{x}_{i-1})\right)$, the operator $\partial\mathcal{K}/\partial\boldsymbol{d}_i$ represents the tangent linearization of 4D-Var for outer-loop *i*, and $(\partial\mathcal{K}/\partial\boldsymbol{d}_i)^T$ is the corresponding adjoint. In the case of a single outer-loop, equation (7) reduces to:

$$\boldsymbol{A}(-\tau) = (\boldsymbol{I} - (\partial\mathcal{K}/\partial\boldsymbol{d})\boldsymbol{H}_b)\boldsymbol{B}(\boldsymbol{I} - (\partial\mathcal{K}/\partial\boldsymbol{d})\boldsymbol{H}_b)^T + (\partial\mathcal{K}/\partial\boldsymbol{d})\boldsymbol{R}(\partial\mathcal{K}/\partial\boldsymbol{d})^T \tag{8}$$

which was the case considered by MAB for estimating the expected analysis error variance of several different circulation indices. Since (7) and (8) are based on a 1$^{\text{st}}$-order linearization of $\mathcal{K}(\boldsymbol{d})$ in (6), it is assumed that the influence of higher-order terms on $\boldsymbol{A}_n(-\tau)$ is negligible. As noted in section 1, the explicit computation of all the elements of $\boldsymbol{A}$ would be prohibitively expensive given the very large dimension of most problems of interest. However, since the matrix in (7) and (8) is available as an operator in the form of FORTRAN code, important properties of the error covariance matrix can be quantified using iterative methods since all that is required is the ability to compute a matrix-vector product.

The tangent linear operator $(\partial\mathcal{K}/\partial\boldsymbol{d})$ and its adjoint $(\partial\mathcal{K}/\partial\boldsymbol{d})^T$ have considerable utility (Moore *et al.,* 2011a). For example, the operators can be used to quantify the sensitivity of the 4D-Var system to uncertainties in the system, provide information about the impact of observations on the analyses and forecast (*e.g.*, Trémolet, 2008), yield information about the expected error variance in scalar functions (MAB), or provide information about the stability and conditioning of the 4D-Var inversion procedure. The latter arises from the useful properties of the tangent linearization and adjoint of the conjugate gradient method (Gratton *et al.,* 2014).

In the investigations described in later sections, it is important to note that $(\partial\mathcal{K}/\partial\boldsymbol{d})$ and $(\partial\mathcal{K}/\partial\boldsymbol{d})^T$ were derived directly from the data assimilation FORTRAN code using standard recipes (*e.g.* Giering and Kaminski, 1998), and each operator represents one complete outer-loop evaluation of the tangent linear and adjoint of the 4D-Var system. Thus, the computational cost of each of these operations is comparable to running 4D-Var. However, (7) represents an explicit operator for the expected analysis error covariance arising from an infinite ensemble, and from which matrix-vector products can be computed. Therefore, various properties of the analysis error covariance matrix, such as the total error variance (*i.e.*, the trace) and Empirical Orthogonal Functions (EOFs), can be computed iteratively.

c. Forecast error covariance

Suppose now that the unperturbed analysis $\boldsymbol{x}^a$ of section 2b is advanced to the end of the analysis window $t = 0$ and used to initialize a forecast denoted $\boldsymbol{x}^f$, as shown schematically in Fig. 1 for the interval $(0, t]$. Similarly, an ensemble of forecasts can be created, each initialized from individual members of the analysis ensemble of section 2b. The covariance of the forecast ensemble about the unperturbed forecast $\boldsymbol{x}^f$ will mimic the covariance of the expected forecast errors. Under this scenario, and neglecting for now model error, a linear approximation of the expected forecast error covariance matrix $\boldsymbol{F}(t)$ during the forecast interval $t = (0, t]$ (illustrated in Fig. 1) is given by:

$$\boldsymbol{F}(t) = \boldsymbol{M_f}(0,t)\boldsymbol{A}_n(0)\boldsymbol{M}_{\boldsymbol{f}}^T(t,0) \qquad (9)$$

where $\boldsymbol{M_f}(0,t)$ denotes the tangent linear model linearized about the forecast $\boldsymbol{x}^f(t)$, $\boldsymbol{M}_{\boldsymbol{f}}^T(t,0)$ is the adjoint model where the reversed arguments indicate integration backward in time over the forecast interval, and $\boldsymbol{A}_n(0)$ is the analysis error covariance matrix at the *end* of the analysis window, $t = 0$ (*cf.*, Fig. 1). In this framework, the unperturbed forecast $\boldsymbol{x}^f$ is equivalent to the ensemble mean, and $\boldsymbol{F}(t)$ is the covariance of the (*infinite*) ensemble about the ensemble mean. The analysis error covariance at $t = 0$ is given by $\boldsymbol{A}_n(0) = \boldsymbol{M_b}(-\tau,0)\boldsymbol{A}_n(-\tau)\boldsymbol{M}_{\boldsymbol{b}}^T(0,-\tau)$ where $\boldsymbol{A}_n(-\tau)$ is the expected analysis error covariance at the *beginning* of the analysis window given by (5), and $\boldsymbol{M_b}(-\tau,0)$ denotes the tangent linear model linearized about the background $\boldsymbol{x}^b$ over the analysis window.

Using (7), the expected forecast error covariance can be computed according to:

$$\boldsymbol{F}_n(t) = \boldsymbol{M}_{\boldsymbol{f}}(0,t)\boldsymbol{M}_{\boldsymbol{b}}(-\tau,0)\boldsymbol{A}_n(-\tau)\boldsymbol{M}_{\boldsymbol{b}}^T(0,-\tau)\boldsymbol{M}_{\boldsymbol{f}}^T(t,0). \qquad (10)$$

The covariance matrices in (3) and (9) are defined in terms of the L2-norm and, as such, cross-covariances between different physical variables of the state vector will have mixed units (*e.g.*, ms^{-1}°C). While this is an acceptable definition of covariance, the mixed units can render difficult a direct comparison of individual matrix elements and complicate the interpretation of the EOFs. Alternatively, a norm can be chosen whereby the elements of the resulting error covariance matrix all have the same units. In numerical weather prediction, it is common to use an energy norm to define the covariance of the forecast error $\boldsymbol{\varepsilon}$ (*e.g.*, Buizza and Palmer, 1995) such that $\boldsymbol{C} = E\{\boldsymbol{U}\boldsymbol{\varepsilon}\boldsymbol{\varepsilon}^T\boldsymbol{U}^T\}$, where $E\{\cdots\}$ denotes the expectation operator, and $\boldsymbol{U}$ is an appropriate weight matrix so that all elements of the vector $\boldsymbol{U\varepsilon}$ have the units of the square root of energy. The choice of an energy norm is also appealing given the fundamental role that energy plays in our understanding of the underlying physical processes that govern the ocean circulation, the very same processes that control the evolution of forecast errors. Therefore, an energy norm, described in appendix A, was used in all of the computations reported here in which $\boldsymbol{U}$ is time-invariant. As in section 2, the various matrix operations in (10) are available as FORTRAN code, and various properties of $\boldsymbol{F}_n(t)$ can be evaluated using iterative methods.

3. Experimental Setup

Attention is confined here to the relatively simple yet dynamically relevant case of the adjustment of an ocean temperature front in a zonally re-entrant channel and the subsequent relaxation toward a restratified water column, a problem that has been studied extensively in the oceanographic literature (*e.g.*, Boccaletti *et al.,* 2007; Klein *et al.,* 2008).

a. Paternal twin models

The model used was the Regional Ocean Modeling System (ROMS; Shchepetkin and McWilliams, 2005). It was configured for a flat-bottomed, zonally periodic channel 1000 km long, 2000 km wide, and 4000 m deep centered on 43.3°S. Two configurations of the model were considered: “Model T” with 2.5 km grid-spacing in the horizontal, and “Model F” with 20 km horizontal grid spacing. In both models, 20 unevenly spaced levels were used in the vertical with spacing ~20 m near the surface, increasing to ~700 m at the bottom. Both models employ 4th-order horizontal and vertical advection for tracers, and 3rd-order upstream horizontal advection for momentum in conjunction with 4th-order vertical advection of momentum. Horizontal mixing in the form of 2nd-order eddy diffusivity and eddy viscosity was used that is parallel to the model σ-levels with coefficients of eddy viscosity and diffusivity of 25 m^2 s^{-1} in Model T and 400 m^2 s^{-1} in Model F. Vertical mixing was parameterized using the $k-\varepsilon$ generic length scale formulation of Umlauf and Burchard (2003) with lower thresholds of 10^{-5} m^2 s^{-1} for the vertical mixing coefficients of tracer and momentum in Model T and 5×10^{-5} m^2 s^{-1} in Model F. The time step in Model T was 150 s compared to 1200 s in Model F.

Model T was used to simulate the true ocean circulation, and following Smith *et al.* (2015; hereafter SMA) was initialized from rest with a meridional temperature front described by $T(y,z) = (T_0 - T_r(y))(1 - (z/H)^{1/2})$ where $T_r(y) = \alpha f(y)\mathrm{erf}((y - y_0)/L)/f_0$, with $\alpha = 4.52$, y is the cross-channel distance, z is depth, $f(y)$ is the Coriolis parameter on a β-plane with a value of f_0 at the central latitude 43.3°S, $L = 80$ km is the meridional scale of the temperature front, H is the channel depth, y_0 is the value of y at the mid-point of the channel, and $T_0 = 12$°C is the surface temperature at y_0. Salinity was not included in the model calculations reported here. Instability growth was encouraged by adding small amplitude, sinusoidal, zonal wavenumber-1 and zonal wavenumber-2 perturbations to the initial condition. For simplicity, there is no surface forcing imposed in either Model T or Model F. However, the instability process was prolonged by weakly relaxing the solution to the initial temperature profile on a time scale of 50 days. Figures 2a-d shows the evolution of the SST of the circulation that develops in Model T between days 50 and 134.

As noted in section 1, fronts are a common feature of the ocean circulation and occur on a wide range of scales ranging from the geostrophic regime down to the sub-mesoscale. Here, we concentrate on the quasi-geostrophic regime, which includes the formation of seasonal fronts such as sub-polar and shelf-break fronts, and upwelling fronts such as those that form in eastern boundary current systems. In the experiments presented here, the presence of the front is taken as a given, and we do not concern ourselves with the mechanism of frontogenesis, although surface forcing is known to play a major role in many instances. For example, cross-front Ekman transport associated with along front winds can hasten the formation or demise of a front depending on the wind direction. Here we simply explore the collapse of a front after genesis, and the subsequent relaxation toward a restratified ocean. With this in mind, Figs. 2a-d illustrate very clearly the complex circulation that develops as a result of the baroclinic instabilities that ensue as the isotherms slump in an attempt to move toward a lower energy state. Initially, the circulation is dominated by the development of a zonal wavenumber-2 instability, which later gives way to a zonal wavenumber-1 feature.

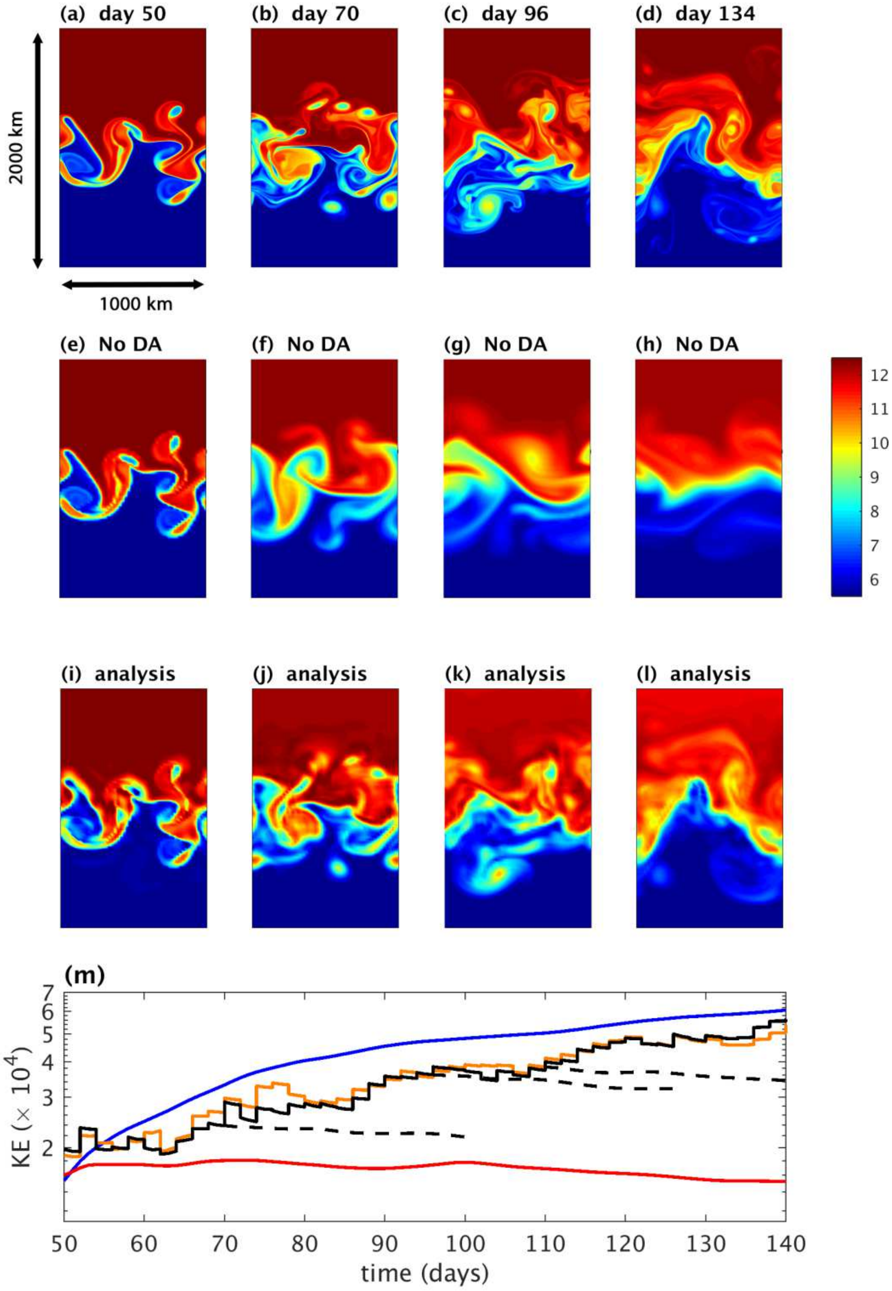

Figure 2: The SST (°C) from the circulation captured by Model T (a-d) and Model F without data assimilation (e-h) on selected days. The day number correspond to each column is indicated in the upper row. The Model F *strong* constraint 4D-Var analyses for the same days are shown in (i-l). (m) Time series of the kinetic energy (m^2s^{-2}) of the vertically integrated velocity are also shown from Model T (blue line), Model F without data assimilation (red line), Model F *strong* constraint 4D-Var analyses (black solid line) and Model F *weak* constraint 4D-Var analyses (orange line). Also shown are kinetic energy time series for 30-day forecasts initialized from the *strong* constraint 4D-Var analysis on days 70, 96, and 110 (black dashed lines).

Model F was used as a surrogate for Model T. Figures 2e-h show the SST from the integration of Model F initialized with the Model T state-vector on day 50 that was first subsampled on the Model F grid. Comparison with Figs. 2a-d indicates that the Model F solution diverges from the parent Model T circulation over time. As anticipated, the Model F solution is less energetic than Model T, as illustrated in Fig. 2m, which shows the time series of the domain-integrated kinetic energy (KE) computed from the vertically integrated velocity. During the period shown, the Model T KE continues on an upward trajectory indicating that the circulation has not yet reached an equilibrium. The available potential energy (APE) is still being converted to KE as the instabilities develop. Conversely, the Model F KE asymptotes quickly and then undergoes a slow decline over time, indicating that, in this case, the conversion of APE to KE is offset by dissipation (recall that there is no surface forcing and the relaxation term is weak).

b. Strong and weak constraint 4D-Var

The Model T circulation between days 50 and 110 (*cf.*, Figs. 2a-d) was used as a surrogate for the true ocean circulation. This 60-day time interval was divided into 2-day windows, and simulated observations (drawn from Model T) during each window were assimilated into Model F using 4D-Var during the resulting 30 analysis cycles. The 4D-Var analysis at the end of each time window was used as the background estimate $\boldsymbol{x}^b$ at the start of the next cycle. The background circulation for the first cycle was chosen to be the Model T circulation on day 49, subsampled on the Model F grid.

The observations were all in the form of vertical profiles of temperature over the upper 1000 m of the water column only, regularly spaced in the horizontal and in time. Observations were available at times corresponding the beginning, middle and end of each 2-day analysis cycle, and sampled every 60 km (corresponding to every third Model F horizontal grid point), yielding ~26,000 observations per 2-day assimilation window. Random observation errors with zero mean and a standard deviation of 0.1ºC were added to each datum. The observation errors were assumed to be mutually uncorrelated, a reasonable assumption for independent vertical profiles, so the observation error covariance matrix $\boldsymbol{R}$ is diagonal. The diagonal elements of $\boldsymbol{R}$ correspond to an error standard deviation of 0.22ºC, a combination of the measurement error and an assumed error of representativeness with a standard deviation of 0.2ºC.

The background error covariance matrix $\boldsymbol{B}$ was estimated using the identical twin experiments described by SMA who used a similar model configuration with 10 km horizontal grid spacing. Specifically, the standard deviations and typical correlation length scales of the background errors were computed from the SMA circulation estimates and then used in the ROMS 4D-Var model for $\boldsymbol{B}$, which is based on the diffusion operator approach of Weaver and Courtier (2001). In addition, the balance operator of Weaver *et al.* (2005) was also employed. Both strong and weak constraint 4D-Var experiments were performed. In the strong constraint case, Model F is assumed to be free of errors, and the 4D-Var control vector comprises only the model initial conditions. However, imperfections in Model F arise from poor horizontal resolution and "errors" associated with imperfect parameterizations. Therefore, in the case of weak constraint 4D-Var, the control vector is augmented with a correction for model error $\boldsymbol{\eta}(t)$ that is applied at every grid point and every time step in Model F. Similarly, the background error covariance matrix $\boldsymbol{B}$ in (2) is replaced by $\boldsymbol{D} = \mathrm{diag}(\boldsymbol{B}, \boldsymbol{Q})$ where $\boldsymbol{Q}$ is the model error covariance matrix.

The matrix $\boldsymbol{Q}$ describes the covariance of typical model errors that develop during each 2-day assimilation cycle. To estimate a time-invariant $\boldsymbol{Q}$, Model F was initialized at the start of each 2-day window with the Model T solution on the same day sub-sampled on the Model F grid. The difference between the Model F solution two days later and the corresponding Model T solution was then used to estimate the standard deviation of the model error and typical correlation length scales, the latter employing the semi-variogram approach of Banerjee *et al.* (2004). In this way, $\boldsymbol{Q}$ represents the statistics of typical model errors that develop during the 2-day assimilation windows. During weak constraint 4D-Var experiments, $\boldsymbol{Q}$ was modeled using a diffusion operator as for $\boldsymbol{B}$. In practice, the control vector corrections $\boldsymbol{\eta}(t)$ for model error were only computed every 2 hours during the weak constraint experiments and linearly interpolated to times in between, so a decorrelation time of 1 day was also assumed for model error to regularize the time evolution of model error corrections. This time scale is consistent with the slow time evolution of the Model F minus Model T differences used to estimate $\boldsymbol{Q}$.

In all experiments, homogeneous, isotropic correlation functions were employed to model $\boldsymbol{B}$ and $\boldsymbol{Q}$. Specifically, for $\boldsymbol{B}$ ($\boldsymbol{Q}$) the following correlation lengths were used: 150 (200) km for the free surface height, 75 (200) km for both horizontal velocity components and 65 (200) km for temperature. A vertical correlation length of 200 m was used for both $\boldsymbol{B}$ and $\boldsymbol{Q}$.

In all experiments, the simulated observations were assimilated into Model F using the dual formulation of *strong* and *weak* constraint 4D-Var described in detail by Moore *et al.* (2011b) and Gürol *et al.* (2014). Figures 2i-l show the Model F SST from the *strong* constraint 4D-Var analyses on selected days. A comparison with the true solution (Figs. 2a-d) confirms that data assimilation can recover the majority of the Model T circulation features that are resolved by the Model F grid. The *weak* constraint circulation analyses are very similar to those in Figs. 2i-l (not shown). Data assimilation also energizes the circulation as shown in Fig. 2m, which shows a time series of KE from both the *strong* and *weak* constraint analyses. During each 4D-Var cycle, APE is added by the observations, thereby propping up the isotherms and leading to elevated KE through baroclinic conversion processes. The discrete jumps in KE between 4D-Var cycles are very evident in Fig. 2m. Furthermore, Fig. 2m also shows that the weak constraint forcing term $\boldsymbol{\eta}(t)$ often further energizes the analyses.

4. Properties of the Error Covariance Matrix

As discussed in section 2, the properties of the analysis and forecast error covariance matrices associated with the Model F experiment are of interest. These provide quantitative information about the veracity of the 4D-Var analyses and ensuing forecasts. In this section, we will first explore some general properties of the expected error covariance matrices arising from the infinite ensemble of perturbed 4D-Var analyses described in sections 2b and 2c. The perturbed 4D-Var analyses are described in appendix B.

a. The determinant

The determinant of a covariance matrix can be expressed as the product of its eigenvalues. Furthermore, the associated eigenvectors define the direction of the semi-major axes of a multi-dimensional hyper-ellipsoid, while the square root of each eigenvalue represents the axes lengths. Therefore, the determinant of the covariance matrix is of interest because it is proportional to the squared-volume of the hyper-ellipsoid. Specifically, the determinant of a covariance matrix is proportional to the squared hyper-volume of all ocean states for which the error is smaller than one standard deviation. Therefore, in the case of the analysis error covariance, a smaller determinant indicates a more precise estimate of the ocean state from the data assimilation system. As shown in section 4c, the temporal evolution of the determinant of a covariance matrix also provides information about the flow of probability through the system. As noted in appendix C, for the large dimension problem considered here (~10^5), it is not practical to explicitly compute the analysis and forecast error covariance matrices. Therefore, as described in appendix C, the determinants of the energy-weighted analysis error covariance matrix $\boldsymbol{U}\boldsymbol{A}_n\boldsymbol{U}^T$ and forecast error covariance matrix $\boldsymbol{U}\boldsymbol{F}_n(t)\boldsymbol{U}^T$ were estimated using the Monte Carlo method of Bai *et al.* (1996), an approach that invokes the Lanczos algorithm (Golub and van Loan, 1989) to estimate the eigenvectors of each matrix iteratively. Also, the Bai *et al.* method places upper and lower bounds on the determinant estimates.

Using the "paternal twin" approach described in section 3, the simulated observations from Model T were assimilated into Model F using a single outer-loop and 25 inner-loops, a choice based on the experience of SMA. Since a single outer-loop is considered, the subscript *n* will be dropped in the sequel. If no data are assimilated, $\boldsymbol{K} = \boldsymbol{0}$ and (3) reduces to $\boldsymbol{A}(-\tau) = \boldsymbol{B}$. The volume of the hyper-ellipsoid $det(\boldsymbol{U}\boldsymbol{B}\boldsymbol{U}^T)^{1/2}$ is, therefore, a useful benchmark. As noted in section 3b, the balance operator of Weaver *et al.* (2005) was also employed in the parameterization of $\boldsymbol{B}$. However, since the balance operator is only weakly flow-dependent, $\boldsymbol{B}$ varies very little from one data assimilation cycle to the next. This is illustrated in Fig. 3a, which shows an estimate of $\ln\left(det(\boldsymbol{U}\boldsymbol{B}\boldsymbol{U}^T)^{1/2}\right)$ (*i.e.*, a measure of the natural log of the hyper-ellipsoid volume) based on the energy norm (black circles). Because of the large dimension of the system considered here (~10^5), the approach is computationally very demanding, so estimates of the determinant were only computed every 4th analysis cycle.

The volume of the hyper-ellipsoid defined by the expected analysis error covariance matrix at the beginning of each analysis cycle (*i.e.*, $t = -\tau$ in Fig. 1) is given up to a constant of proportionality by $det(\boldsymbol{U}\boldsymbol{A}(-\tau)\boldsymbol{U}^T)^{1/2}$. A time series of $\ln\left(det(\boldsymbol{U}\boldsymbol{A}(-\tau)\boldsymbol{U}^T)^{1/2}\right)$ is shown in Fig. 3a (dark blue circles) for every 4th *strong* constraint 4D-Var cycle and indicates that the analysis error covariance hyper-ellipsoid volume at time $t = -\tau$ is indistinguishable from that associated with $\boldsymbol{B}$.

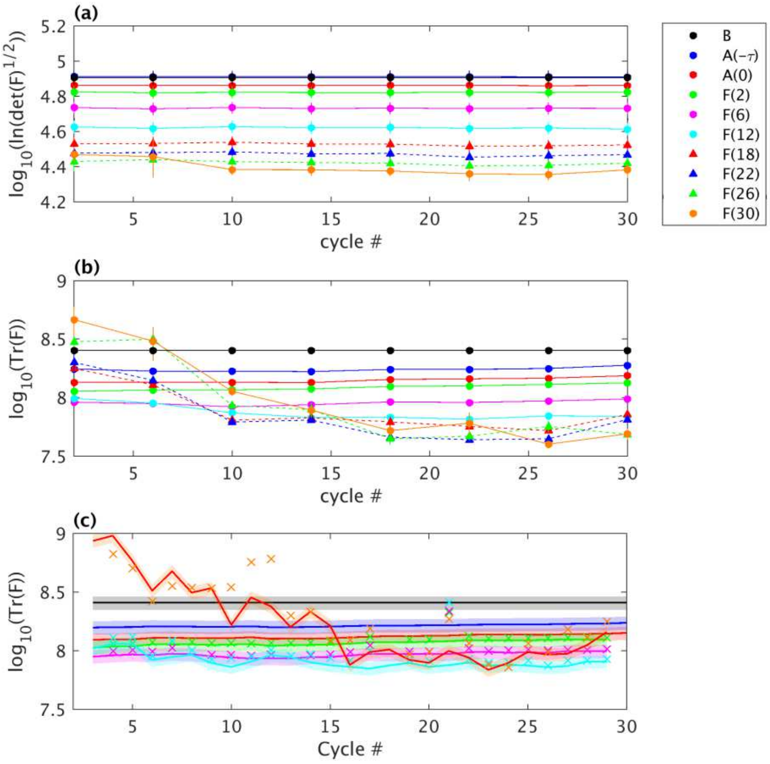

Figure 3: (a) Times series of $\log_{10}\left(\ln\left(det(\boldsymbol{UBU}^T)^{1/2}\right)\right)$ (black circles and black line), $\log_{10}\left(\ln\left(det(\boldsymbol{UA}(-\tau)\boldsymbol{U}^T)^{1/2}\right)\right)$ (blue circles and blue line), $\log_{10}\left(\ln\left(det(\boldsymbol{UA}(0)\boldsymbol{U}^T)^{1/2}\right)\right)$ (red circles and red line) and $\log_{10}\left(\ln\left(det(\boldsymbol{UF}(t)\boldsymbol{U}^T)^{1/2}\right)\right)$ for various forecast lead times: $t = 2$ days (green circles and green line), $t = 6$ days (magenta circles and magenta line), $t = 12$ days (cyan circles and cyan line), $t = 18$ days (red triangles and red dashed line), $t = 22$ days (blue triangles and blue dashed line), $t = 26$ days (green triangles and green dashed line), and $t = 30$ days (orange circles and orange line). Values were computed for every 4th analysis cycle (*i.e.*, every 8 days). The upper and lower bounds associated with each estimate are indicated by the vertical error bars, although in most cases, these are too small to be visible. (b) Times series of $\log_{10}\left(tr(\boldsymbol{UBU}^T)\right)$, $\log_{10}\left(tr(\boldsymbol{UA}(-\tau)\boldsymbol{U}^T)\right)$, $\log_{10}\left(tr(\boldsymbol{UA}(0)\boldsymbol{U}^T)\right)$, and $\log_{10}\left(tr(\boldsymbol{UF}(t)\boldsymbol{U}^T)\right)$ for the same lead-times shown in (a). The color-coding is the same as in (a) and indicated in the legend. (c) Time series of trace estimates based on a randomization method for a subset of the forecast lead times shown in (b) and computed for every analysis cycle (*i.e.*, every 2 days). The shaded regions indicate the corresponding uncertainty of ±13% based on the sample size of random vectors used. The crosses (×) show the corresponding randomized trace estimates of the expected $\boldsymbol{UFU}^T$ for forecasts initialized from *weak* constraint 4D-Var analyses. The color-coding is the same as in (a) and (b) and indicated in the legend.

Figure 3a (red circles) also shows a time series of the hyper-ellipsoid volume defined by the expected analysis error variance at the end of the same *strong* constraint 4D-Var cycles (*i.e.*, $t = 0$) which is given by $det(\boldsymbol{UA}(0)\boldsymbol{U}^T)^{1/2} = det(\boldsymbol{UM_b}(0,-\tau)\boldsymbol{A}(-\tau)\boldsymbol{M}_{\boldsymbol{b}}^T(-\tau,0)\boldsymbol{U}^T)^{1/2}$. The volume of the error hyper-ellipsoid subspace can be seen to decrease in time during the analysis window.

Following the usual operational practice, the *strong* constraint 4D-Var analyses at the end of each analysis cycle ($t = 0$ in Fig. 1) were used as the initial conditions for each forecast cycle. Figure 3a also shows time series of the hyper-ellipsoid volume defined by the expected forecast error covariance $\boldsymbol{UF}(t)\boldsymbol{U}^T$ for forecast lead times t of 2 (green circles), 6 (magenta circles), 12 (cyan circles), 18 (red triangles), 22 (blue triangles), 26 (green triangles) and 30-days (orange circles) duration. Figure 3a indicates that the forecast error covariance hyper-ellipsoid volume generally collapses as the forecast lead time increases. The exception is early on in the analysis-forecast experiment during cycles 2 and 6, where there is an indication that the 30-day forecast error hyper-ellipsoid expands again, although for this case Fig. 3a indicates that the uncertainties are larger. The properties of the circulation through time associated with this behavior will be explored later. Another remarkable feature of Fig. 3a is that for a given lead time, the hyper-ellipsoid volume varies very little from cycle-to-cycle, excepting the 30-day forecasts. The generally observed collapse of the hyper-ellipsoid volume is consistent with a slow decline in the forecast circulation energy, as illustrated in Fig. 2m, which shows time series of KE for three representative cases. In each example, the KE slowly decreases over time and is at all times lower than that of the 4D-Var analysis on the same day.

b. The trace

The trace of the leading diagonal of the energy-weighted analysis error covariance matrix $\boldsymbol{UAU}^T$ and forecast error matrix $\boldsymbol{UF}(t)\boldsymbol{U}^T$ represents the expected total error variance in each case. The trace of a matrix can additionally be expressed as the sum of the eigenvalues. The trace of each covariance matrix was also estimated iteratively using the method of Bai *et al.* (1996), and time series are shown in Fig. 3b for every 4th analysis-forecast cycle. The trace estimates generally converge faster than the estimates of the determinant, which is reflected in the smaller error bars in Fig. 3b.

Figure 3b suggests two different types of behavior for the total variance. During the first 10-15 cycles, the total error variance decreases steadily from the background value, through the analysis cycle, and out to around forecast day 6-12, after which error variance increases again with increasing forecast lead time. Thus, during these cycles, while the volume of the hyper-ellipsoid is collapsing (*cf.*, Fig. 3a), it is becoming very elongated in the direction of some semi-major axes. Conversely, after cycle 15, Fig. 3b shows that the total error variance generally decreases out to around forecast day 22, and significant elongation of the hyper-ellipsoid is delayed. The mechanics of this behavior are explored further in section 5.

While it is computationally prohibitive to compute trace estimates for every analysis-forecast cycle using the method of Bai *et al.* (1996), a less demanding approach can be used based on a *randomized trace estimate method* described by Fisher and Courtier (1995). In this case, an estimate of the trace of the positive-definite matrix $\boldsymbol{C}$ can be computed according to $tr(\boldsymbol{C}) \approx (1/M)\sum_{i=1}^{M} \boldsymbol{v}^T\boldsymbol{C}\boldsymbol{v}$, where $\boldsymbol{v}$ is a random vector drawn from the normal distribution $N(0,1)$, and M is the sample size. While this procedure is computationally less demanding than the method of Bai *et al.* (1996), the resulting trace estimates are less accurate. Nonetheless, they provide useful information about the behavior of the total error variance during *all* cycles. The percentage expected error in the trace estimate, in this case, is given by $100/(2M)^{1/2}$. In the following examples, $M = 30$ which yields trace estimates with an expected error ~13%, which is deemed adequate for exploring the general behavior of the total error variance since the trace estimates for different lead times are distinguishable. The relative performance of the two trace estimation methods employed in this study is further documented in appendix C.

Time series of the trace estimates using the alternative *randomized trace estimate* approach are shown in Fig. 3c for every 2-day *strong* constraint analysis-forecast cycle, and confirm the same general behavior noted above. Figure 3c also shows the total expected forecast error variance for forecasts initialized by analyses computed using *weak* constraint 4D-Var. In general, the forecast error variance displays behavior that is similar to forecasts initialized from the strong constraint analyses. However, there are some cycles where the response is quite different (*e.g.*, the 30-day forecasts for cycles 10-15). As noted earlier, Fig. 2m indicates that the *weak* constraint circulation estimates are frequently more energetic than their *strong* constraint counterparts. It is, therefore, reasonable to assume that during such times the model error forcing $\boldsymbol{\eta}(t)$ provides additional APE during the analysis cycle that, in turn, yields a more unstable forecast state and larger forecast error variance.

c. The flow of probability

The time evolution of the determinant of a covariance matrix provides quantitative information about the flow of probability through the analysis-forecast system. Following the notation introduced in section 2a, the time evolution of the forecast state-vector $\boldsymbol{x}^f$ can be represented as $d\boldsymbol{x}^f/dt = \mathcal{M}(\boldsymbol{x}^f)$ where $\mathcal{M}$ represents the non-linear ROMS model. If, as before, $\boldsymbol{\varepsilon}(t)$ denotes the error in the forecast, then to 1st-order:

$$d\boldsymbol{\varepsilon}/dt = \boldsymbol{\Phi_f}(t)\boldsymbol{\varepsilon}(t) + \boldsymbol{\varsigma}(t) \qquad (11)$$

where $\boldsymbol{\Phi_f} = (\partial\mathcal{M}/\partial\boldsymbol{x})|_{x^f}$ is the Jacobian of $\mathcal{M}$ describing the tangent linearization of $\mathcal{M}$ about $\boldsymbol{x}^f$, and $\boldsymbol{\varsigma}(t)$ represents model error. Ideally, $\boldsymbol{\Phi_f}$ would represent a linearization of $\mathcal{M}$ about the true state, which, of course, is never known. However, as discussed in section 2b, the evolution of perturbations around the reference forecast $\boldsymbol{x}^f$ are used as a surrogate for describing forecast errors, in which case $\boldsymbol{x}^f$ represents the ensemble mean (or more formally the expected value of $\boldsymbol{x}$), and $\boldsymbol{\Phi_f}$ describes the time evolution of each member of the infinite ensemble of perturbations $\boldsymbol{\varepsilon}(t)$.

It is well known (Gardiner, 1985) that the probability density function (pdf) of the forecast errors $\boldsymbol{\varepsilon} = (\varepsilon_i)$ in (11) is described by the Fokker-Planck equation:

$$\partial p/\partial t = -\sum_{i=1}^{N} \partial(a_i p)/\partial\varepsilon_i + \tfrac{1}{2}\sum_{i=1}^{N}\sum_{j=1}^{N} \partial^2\big(q_{i,j}p\big)/\partial\varepsilon_i\partial\varepsilon_j \qquad (12)$$

where $p \equiv p(\boldsymbol{\varepsilon}(t)|\boldsymbol{\varepsilon}(0))$ is the conditional probability of the error $\boldsymbol{\varepsilon}(t)$ given the initial condition $\boldsymbol{\varepsilon}(0)$, a_i are the elements of the vector-field $\boldsymbol{a}(t)$ generated by $\boldsymbol{\Phi_f}$ (*i.e.*, $\boldsymbol{a}(t) \equiv d\boldsymbol{\varepsilon}/dt = \boldsymbol{\Phi_f}\ (t)\boldsymbol{\varepsilon}(t)$), and $q_{i,j}$ are the elements of the model error covariance matrix $\boldsymbol{Q} = E\{\boldsymbol{\varsigma}\boldsymbol{\varsigma}^T\}$. By analogy with the advection-diffusion equation, $\boldsymbol{a}(t)$ plays the role of a *velocity* that advects the mean of the pdf through state-space and is commonly referred to as the *drift* vector or *drift* velocity. Since, in general, the divergence of the drift velocity does not vanish, $\boldsymbol{a}(t)$ will also influence the "width" of the pdf. The second term on the right-hand side of (12) is associated with the stochastic forcing $\boldsymbol{\varsigma}(t)$ in (11) and is referred to as *diffusion* since $\boldsymbol{Q} = \big(q_{i,j}\big)$ acts like a diffusion matrix that "broadens" the pdf. Following Gardiner (1985), (12) can be recast as $\partial p/\partial t = -\sum_{i=1}^{N} \partial \boldsymbol{C}_i/\partial \varepsilon_i$ where the vector $\boldsymbol{C}_i = \boldsymbol{a}(t)p - \frac{1}{2}\sum_{j=1}^{N} \partial\left(q_{i,j}p\right)/\partial \varepsilon_j$ is a *probability current* and $\sum_{i=1}^{N} \partial \boldsymbol{C}_i/\partial \varepsilon_i$ is the total divergence.

The presence of stochastic model error $\boldsymbol{\varsigma}(t)$ is only considered during the analysis cycle in the case of *weak* constraint 4D-Var. Since no allowance is made here for model error during a forecast, it does not factor into the covariance calculations based on (7). Thus, we will drop the *diffusion* term from further analysis. In this case, $\boldsymbol{Q} = \boldsymbol{0}$ and the time evolution of the forecast error covariance matrix $\boldsymbol{UF}(t)\boldsymbol{U}^T = E\{\boldsymbol{U\varepsilon}(t)\boldsymbol{\varepsilon}^T(t)\boldsymbol{U}^T\}$ is given by:

$$d(\boldsymbol{UFU}^T)/dt = \left(\boldsymbol{U\Phi_f U}^{-1}\right)(\boldsymbol{UFU}^T) + (\boldsymbol{UFU}^T)\left(\boldsymbol{U\Phi_f U}^{-1}\right)^T. \qquad (13)$$

Using Jacobi's formula $d\left(det(\boldsymbol{UFU}^T)\right)/dt = tr[adj(\boldsymbol{UFU}^T)\, d(\boldsymbol{UFU}^T)/dt]$, the cyclic properties of the trace, and the associative property of determinants it can be shown that:

$$d\left(\ln\left(det(\boldsymbol{F})^{1/2}\right)\right)/dt = tr\left(\boldsymbol{\Phi_f}(t)\right) \qquad (14)$$

which relates the time rate of change of the volume of the hyper-ellipsoid defined by the forecast error covariance to the trace of the tangent linear model. Note that the result expressed by (14) is independent of the choice of $\boldsymbol{U}$ by virtue of the similarity invariance of $\boldsymbol{U\Phi_f U}^{-1}$.

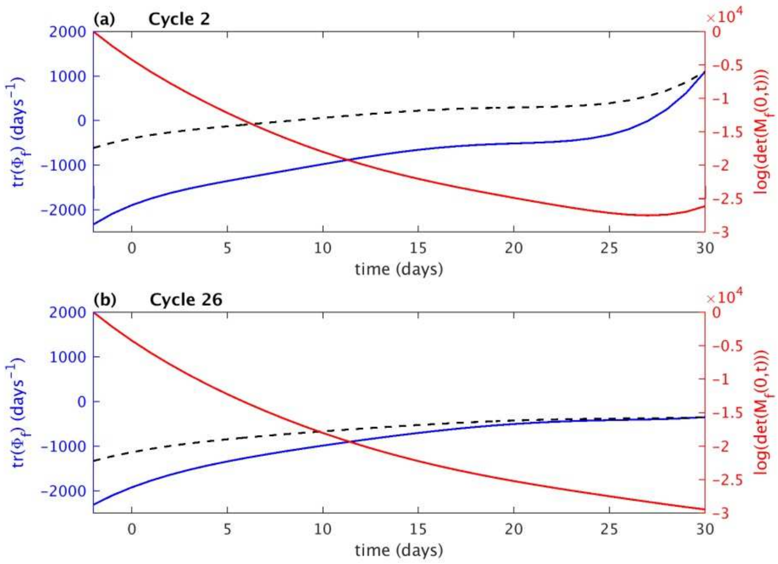

Figure 4: Times series of $tr(\boldsymbol{\Phi_f})$ (blue lines) based on $d\left(\ln\left(det(\boldsymbol{F})^{1/2}\right)\right)/dt$ using (14) for (a) cycle 2 and (b) cycle 26. Time series of $\ln\left(det\left(\boldsymbol{M}_f(0,t)\right)\right)$ are also shown (red lines) for the same cycles. Also shown are time series of $d\left[\ln\left(det\left(\boldsymbol{F}(30,t')\right)\right)\right]/dt$ versus lag time t' for both cycles (black dashed lines) for the lagged forecast error covariance matrix $\boldsymbol{F}(t,t')$. The scale for $d\left[\ln\left(det\left(\boldsymbol{F}(30,t')\right)\right)\right]/dt$ is on the right-hand side, and the abscissa is now interpreted as t'.

Choosing $q_{i,j} = 0$ in (12) leads to Liouville's equation, where the rate of change of the pdf depends only on the *drift* velocity $\boldsymbol{a}(t) = \boldsymbol{\Phi_f}\,(t)\boldsymbol{\varepsilon}(t)$. The total divergence of the *drift* velocity is given by $\sum_{i=1}^{N} \partial a_i / \partial \varepsilon_i = tr\left(\boldsymbol{\Phi_f}\right)$, which according to (14), controls the rate of change of volume of the hyper-ellipsoid associated with the forecast error covariance matrix. To illustrate this result, Figs. 4a and 4b show time series of $tr\left(\boldsymbol{\Phi_f}\right)$ based on (14) for cycles 2 and 26 near the beginning and end of the experiment period, respectively. The time rate of change of $\ln\left(det(\boldsymbol{F})\right)$ was estimated by fitting a 6th-order polynomial to the data in Fig. 3a[1]. As shown in Fig. 3a, the hyper-ellipsoid volume collapses over time through to a forecast lead time ~25-days. Thus, in both cases, $tr\left(\boldsymbol{\Phi_f}\right) < 0$ through forecast lead time of ~25-days indicating that the *drift* velocity $\boldsymbol{a}(t)$ associated with the probability current is convergent, although the rate of convergence decreases with increasing lead time. This suggests that probability becomes more concentrated in state-space as the forecast lead time increases, consistent with a collapse of the pdf. In other words, the volume of the sub-space occupied by all possible forecast errors $\boldsymbol{\varepsilon}(t)$ is also decreasing. This will be further quantified shortly. While the *drift* velocity remains convergent beyond day 25 during cycle 26, Fig. 4a shows that it eventually becomes divergent in the case of cycle 2 (consistent with Fig. 3a), indicating that the probability density begins to decrease as the forecast error hyper-ellipsoid subsequently expands.

d. State-space volume

In the absence of stochastic model error (*i.e.*, $\boldsymbol{\varsigma}(t) = 0$), solutions of (11) can be written in a compact form as $\boldsymbol{\varepsilon}(t) = \boldsymbol{M_f}(0,t)\boldsymbol{\varepsilon}(0)$ where $\boldsymbol{M_f}(0,t)$ is the tangent linear propagator matrix introduced in section 2a. Similarly, the forecast error covariance matrix can be expressed as $\boldsymbol{UF}(t)\boldsymbol{U}^T = \boldsymbol{UM_f F}(0)\boldsymbol{M_f^T U}^T$. Based on the associative property of determinants, it is easy to show that:

$$\ln\left(det\left(\boldsymbol{M_f}(0,t)\right)\right) = \frac{1}{2}\ln\left[det\left(\boldsymbol{F}(t)\right)/det\left(\boldsymbol{F}(0)\right)\right]. \qquad (15)$$

Geometrically, any matrix can be viewed as transforming a unit volume multi-dimensional hyper-cube into a multi-dimensional parallelepiped which, in turn, is defined by the *rows* of the matrix. The determinant of a matrix is then the volume of the resulting parallelepiped. Thus, $det\left(\boldsymbol{M_f}(0,t)\right)$ in (15) represents the volume of state-space occupied by the forecast errors $\boldsymbol{\varepsilon}(t)$. It also follows from (14) and (15) that $det\left(\boldsymbol{M_f}(0,t)\right) = \exp\left(\int_0^t tr\left(\boldsymbol{\Phi_f}(\tau)\right)d\tau\right)$, which is another form of the Liouville equation (Arnold, 1998). Figures 4a and 4b show the time series of $\ln\left(det\left(\boldsymbol{M_f}(0,t)\right)\right)$ for cycles 2 and 26, respectively. In both cases, the volume of state-space occupied by the forecast errors decreases with increasing lead time, although, for cycle 2, there are signs of an increasing tendency around day 28 consistent with the transition in the *drift* velocity from convergent to divergent conditions. Therefore, the sub-space where the forecast

[1] From the associative properties of the determinant, $d\left(\ln\left(det(\boldsymbol{UFU}^T)^{1/2}\right)\right)/dt = \frac{1}{2}d\left(\ln\left(det(\boldsymbol{U})^2 det(\boldsymbol{F})\right)\right)/dt = \frac{1}{2}d\left(2\ln\left(det(\boldsymbol{U})\right) + \ln\left(det(\boldsymbol{F})\right)\right)/dt = d\left(\ln\left(det(\boldsymbol{F})^{1/2}\right)\right)/dt$ for the case here where $\boldsymbol{U}$ is a time-invariant diagonal matrix.

errors reside becomes more certain, in line with the concentration of probability and the collapse of the forecast error covariance hyper-ellipsoid.

5. Empirical Orthogonal Functions

In this section, the topology of the space described by the expected analysis and forecast error covariance matrices is explored.

a. Geometric interpretation

The directions in state-space of the semi-major axes of the hyper-ellipsoids discussed in section 4 are represented by the eigenvectors of the error covariance matrices $\boldsymbol{UAU}^T$ and $\boldsymbol{UF}(t)\boldsymbol{U}^T$. These same eigenvectors are more commonly referred to as Empirical Orthogonal Functions (EOFs), and the associated eigenvalues represent the error variance explained by each EOF. In the present case, the dimension *N* of the hyper-ellipsoid is O(10^5), which would also be the total number of EOFs. The EOF spectrum for either $\boldsymbol{UAU}^T$ or $\boldsymbol{UF}(t)\boldsymbol{U}^T$ can be calculated iteratively using the Lanczos algorithm (Golub and van Loan, 1989). While the Lanczos algorithm can provide an estimate of the entire EOF spectrum, the leading members of the spectrum typically emerge to acceptable precision first when the number of iterations is much less than *N*. Therefore, this is a convenient way to reliably calculate the leading EOFs.

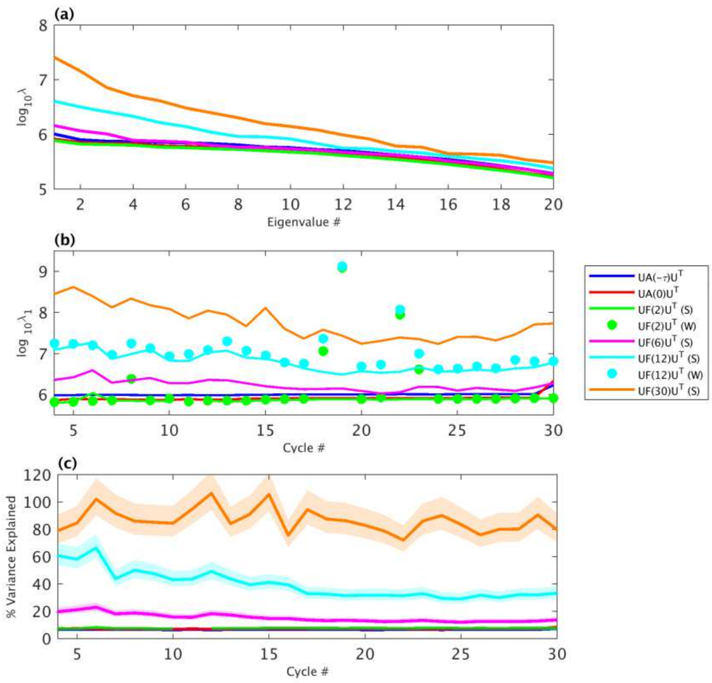

Figure 5: (a) Log_{10} of the leading 20 eigenvalues λ of $\boldsymbol{UA}(-\tau)\boldsymbol{U}^T$, $\boldsymbol{UA}(\boldsymbol{0})\boldsymbol{U}^T$, and $\boldsymbol{UF}(t)\boldsymbol{U}^T$for various forecast lead times, t, for cycle 25. (b) Time series of $\log_{10}(\lambda_1)$ of $\boldsymbol{UA}(-\tau)\boldsymbol{U}^T$, $\boldsymbol{UA}(\boldsymbol{0})\boldsymbol{U}^T$, and $\boldsymbol{UF}(t)\boldsymbol{U}^T$ for various forecast lead time, t, for each cycle. The solid lines are cases for forecasts initialized from *strong* constraint (S) 4D-Var analyses, while the circles (•) are for forecasts initialized from *weak* constraint (W) analyses. (c) The fraction of total variance explained by the leading 30 EOFs of $\boldsymbol{UA}(-\tau)\boldsymbol{U}^T$, $\boldsymbol{UA}(0)\boldsymbol{U}^T$, and $\boldsymbol{UF}(t)\boldsymbol{U}^T$ for various forecast lead times, t, for each cycle. The shading indicates the expected uncertainty of ±13% based on randomized trace estimates of the total variance. The error covariances are based on strong constraint 4D-Var.

Figure 5a shows the eigenvalues associated with the leading 20 EOFs of the expected analysis error covariance matrix at the beginning (dark blue line) and end (red line) of a representative *strong* constraint analysis cycle. In both cases, the leading portion of the EOF spectrum is quite flat. Also shown in Fig. 5a are the eigenvalues of the leading EOFs of the expected forecast error covariance for 2, 6, 12, and 30 day forecast lead times. As the forecast lead time increases, Fig. 5a reveals that the EOF spectrum becomes increasingly peaked, with the leading EOF accounting for a larger fraction of the total variance.

Figure 5b shows the eigenvalue λ_1 associated with the leading EOF of $\boldsymbol{UA}(-\tau)\boldsymbol{U}^T$, $\boldsymbol{UA}(0)\boldsymbol{U}^T$, and $\boldsymbol{UF}(t)\boldsymbol{U}^T$ for t =2-30 days for each cycle. For most cycles, it is apparent that the amplitude of the leading eigenvalue decreases through the analysis cycle from $t = -\tau$ to $t = 0$ and through the forecast cycle to t =2 days. For $t > 2$ days, the leading eigenvalue increases with lead time. Also shown in Fig. 5b are the leading eigenvalues of $\boldsymbol{UF}(t)\boldsymbol{U}^T$ for 2- and 12-day forecasts initialized with *weak* constraint 4D-Var analyses. The behavior is similar to that of the *strong* constraint cases, although again, some cycles (18, 19, and 23) are remarkably different. As noted in section 4b, the *weak* constraint 4D-Var corrections for model error $\boldsymbol{\eta}(t)$ applied during the analysis cycle tend to energize further the forecast initial conditions (*cf.*, Fig. 2m), which in turn can influence the EOF spectrum.

The cumulative variance explained by the leading 30 EOFs of the expected analysis and forecast error covariance is shown in Fig. 5c for each *strong* constraint 4D-Var analysis-forecast cycle. In each case, the randomized trace estimates of the total expected error variance from section 4b were used, and error bounds are also indicated in Fig. 5c based on the expected 13% error in the trace estimates. Figure 5c shows that the fraction of variance explained by the leading EOFs is typically low during the analysis cycle and for short forecast lead times. This is consistent with the relatively flat nature of the spectrum (Fig. 5a). However, the fraction of the total variance explained typically increases with increasing forecast lead time, and for t =30 days is close to 100%. Figure 5c shows that while during some cycles, the cumulative variance explained for the t =30 days case appears to exceed 100%, the error bars in Fig. 5c indicate this can be attributed to the uncertainty in the total variance estimates. Additional calculations for selected cycles suggest that the fraction of explained error variance increases very slowly beyond the leading 30 or so EOFs (not shown).

The results presented here indicate that even though the hyper-ellipsoid volume is collapsing as the forecast lead time increases (*cf.*, Fig. 3a), it is not collapsing uniformly in all directions. In fact, it is becoming more elongated along the directions described by the leading few EOFs (*cf.*, Fig. 5b). Furthermore, as the forecast lead time increases, most of the forecast error is described by a small number of growing directions (*cf.*, Fig. 5c). This agrees with experience in numerical weather prediction (*e.g.*, Phillips, 1986; Houtekamer, 1993).

b. Error structures

The sea surface temperature structure of the leading EOF at each stage of the analysis and forecast cycle for various lead times is shown in Fig. 6 for cycle 6 (using *strong* constraint 4D-Var). The SST analysis for this cycle is also indicated for reference in Fig. 6a. Figure 6b shows that the leading EOF at the beginning of the analysis window ($t = -\tau$ in Fig. 1) comprises coherent mesoscale structures. However, this EOF accounts for only ~0.5% of the total expected analysis error variance in the subspace constrained by 4D-Var on this day. By the end of the analysis cycle ($t = 0$ in Fig. 1), the influence of the time evolution of the circulation on the leading covariance structure is evident in Fig. 6c. At this time, the EOF comprises generally smaller scale structures that wrap around the meanders and eddies of the circulation, although the explained variance is still only ~0.5%. As the forecast lead time increases, Fig. 6 shows that the horizontal scale of the leading EOFs decreases even further, targeting specific areas of the evolving meanders in the circulation that are evident in the analysis of Fig. 6a. Furthermore, the fraction of the variance explained by the leading EOF increases with forecast lead time, and in the case of a 30-day forecast (Fig. 6g) it is 42% for this particular cycle.

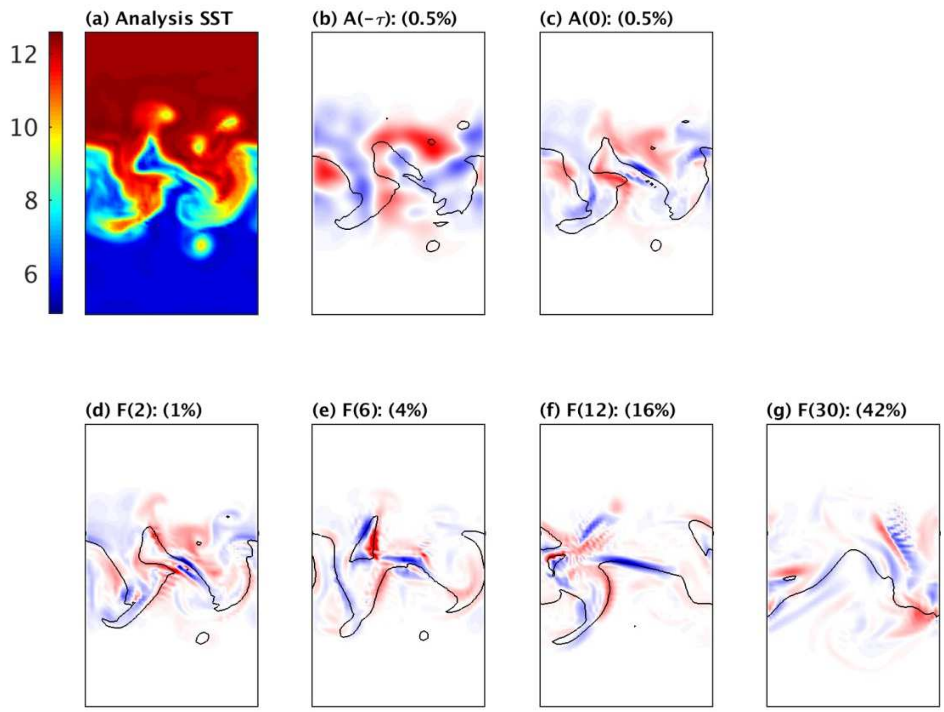

Figure 6: (a) SST analysis for cycle 6 (Celcius). The SST structure of the leading EOF for (b) $\boldsymbol{UA}(-\tau)\boldsymbol{U}^T$, (c) $\boldsymbol{UA}(0)\boldsymbol{U}^T$, (d) $\boldsymbol{UFU}^T$ for t =2 days, (e) $\boldsymbol{UFU}^T$ for t =6 days, (f) $\boldsymbol{UFU}^T$for t =12 days, and (g) $\boldsymbol{UFU}^T$for t =30 days. The percentage variance explained by the leading EOF is also indicated. The 9ºC isotherm on the appropriate analysis or forecast day is also shown (black line) as an indicator of the temperature front position. The error covariances are based on *strong* constraint 4D-Var. In (b)-(g) red indicates positive values and blue indicates negative values.

The leading EOFs of $\boldsymbol{UFU}^T$ can also account for much of the *actual* measured forecast error variance and structure. For example, Figs. 7a-d shows the spatial distribution of the rms forecast errors for 12-day forecasts initialized from the strong constraint 4D-Var analyses from cycles 21-30. The forecast errors are computed relative to the 4D-Var analysis valid on the forecast day. Also shown in Figs. 7e-h is the forecast error explained by the leading 30 EOFs of the expected forecast error covariance matrix $\boldsymbol{UFU}^T$. While the amplitude of the error is underestimated, it is clear much of the structure of the actual forecast errors is captured by the leading 30 EOFs, even though they only capture ~40% of the total variance (*cf.*, Fig. 5c).

c. Forecast error variance as a predictor of forecast skill

In operational ensemble numerical weather prediction systems, the spread of the ensemble about the ensemble mean is used as a surrogate for the forecast error variance (Epstein, 1969; Leith, 1974) and can be of considerable utility because, under some circumstances, it can be used as a predictor of the skill of the ensemble mean (*e.g.*, Barker, 1991; Molteni *et al.*, 1996). Specifically, if the ensemble spread is small (large), this can be an *a priori* indicator of a skillful (unskillful) forecast. However, identification of robust forecast spread-skill relationships (so-called "reliability") has generally proved elusive because such a relationship can depend on many factors. For a perfect forecast model, statistical considerations indicate that ensemble spread is only a good predictor of skill in cases where day-to-day variations in the spread are significant compared to the climatological variance (Houtekamer, 1993; Whitaker and Loughe, 1998). However, even in this case, the maximum correlation between the spread and skill that one can expect is ~0.8. Conversely, when the day-to-day variations in ensemble spread are small compared to climatology, there is generally a very low correlation between spread and skill. The correlation between ensemble spread and forecast skill also depends on the choice of metrics used (Hopson, 2014). Furthermore, imperfections in the forecast model compound the problem, and it is generally necessary to "calibrate" the ensemble in some way to account for the influence of model error. A review of the extensive literature on ensemble numerical weather prediction reveals a range of experiences regarding the relationship between spread and skill (see Grimit and Mass, 2007, for a review).

As noted in sections 2b and 2c, for the experimental set-up considered here, $\boldsymbol{x}^f$ represents the mean of an infinite ensemble of forecasts (*i.e.*, the expected value of $\boldsymbol{x}$). Thus, it is of interest to explore the extent to which the forecast error variance given by the diagonal elements of $(\boldsymbol{UF}(t)\boldsymbol{U}^T)$ (aka the "spread") can be used as a predictor of the skill of $\boldsymbol{x}^f$. Figures 7i-l show the total expected error variance (*i.e.*, spread) in 12-day forecasts initialized from the *strong* constraint 4D-Var analyses of cycles 21-30, based on the leading 30 EOFs of the forecast error covariance matrix. A comparison with Figs. 7a-d indicates that, by-and-large, regions of high spread generally correspond to areas where the forecast errors are largest. While the agreement is not perfect, it is encouraging. Further investigation is warranted to more formally quantify the relationship between forecast skill and expected forecast error variance for the circulation environment considered here. This will be the subject of a future study.

6. Non-Normal and Modal Error Growth

a. Hessian singular vectors

Following Ehrendorfer and Tribbia (1997), the EOFs of the forecast error covariance matrix $\boldsymbol{UF}(t)\boldsymbol{U}^T$ are, in fact, the left singular vectors of the matrix $\boldsymbol{L}(t) = \boldsymbol{UM_f}(0,t)\boldsymbol{A}(0)^{1/2}$, where recall that $\boldsymbol{M_f}(0,t)$ is the propagator of the tangent linear model linearized about the forecast $\boldsymbol{x}^f$ (see Fig. 1). Singular value decomposition of $\boldsymbol{L}$ yields:

$$L^T \psi_i = \lambda_i^{1/2} \hat{s}_i \tag{16}$$
$$L \hat{s}_i = \lambda_i^{1/2} \psi_i$$

where $\boldsymbol{\psi}_i$ represent the EOFs, and $\hat{\boldsymbol{s}}_i$ are the right singular vectors. Introducing the scaled singular vector $\boldsymbol{s}_i = \boldsymbol{A}(0)^{1/2}\hat{\boldsymbol{s}}_i$, the associated eigenvalue problem for $\boldsymbol{s}_i$ becomes $\boldsymbol{M}_f^T(t,0)\boldsymbol{U}^T\boldsymbol{U}\boldsymbol{M}_f(0,t)\boldsymbol{s}_i = \lambda_i \boldsymbol{A}(0)^{-1}\boldsymbol{s}_i$ subject to the orthonormality condition $\boldsymbol{s}_i^T\boldsymbol{A}(0)^{-1}\boldsymbol{s}_j = \delta_{i,j}$, where $\delta_{i,j}$ is the Kronecker delta-function. The vectors $\boldsymbol{s}_i$ are referred to as the Hessian singular vectors (Barkmeijer *et al.,* 1998), so-called because $\boldsymbol{A}(-\tau)^{-1}$ is the Hessian of the 4D-Var cost function. For convenience, the name is carried over here to $\boldsymbol{A}^{-1}$ at other times during the analysis window. From the orthonormality condition, the Hessian singular vectors $\boldsymbol{s}_i$ define a unit hyper-sphere at the forecast start time $t = 0$. However, during the forecast interval, the Hessian singular vectors evolve into the EOFs according to $\boldsymbol{\psi}_i = \lambda_i^{-1/2}\boldsymbol{U}\boldsymbol{M}_f(0,t)\boldsymbol{s}_i$, and the unit hyper-sphere evolves into the hyper-ellipsoid described by the forecast error covariance discussed in section 4.

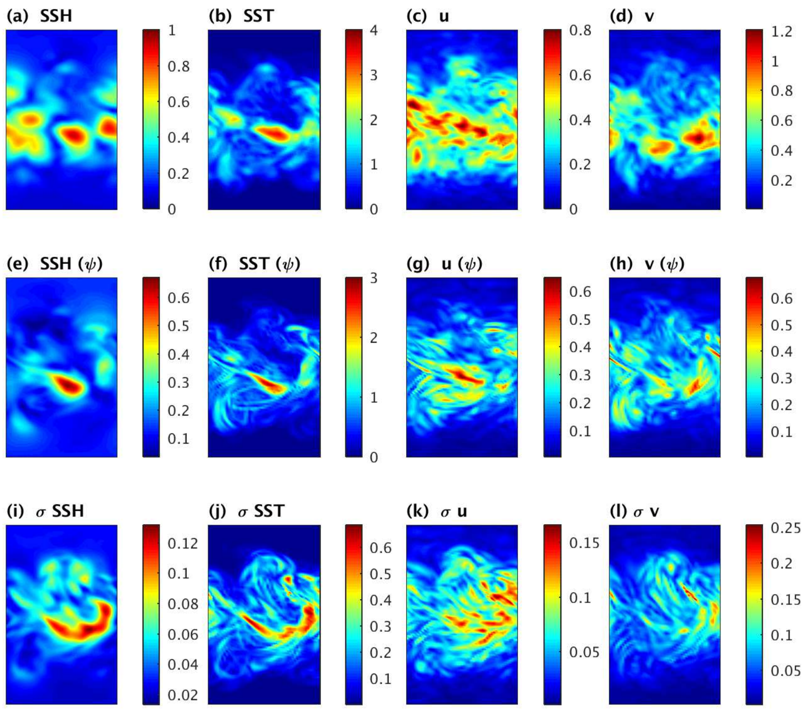

Figure 7: The rms error in (a) SSH (m), (b) SST (°C), (c) surface u (ms^{-1}) and (d) surface v (ms^{-1}) relative to the 4D-Var analysis valid on the same day for 12-day forecasts and averaged over cycles 21-30. The rms errors for the corresponding fields that are explained by the leading 30 EOFs, $\boldsymbol{\psi}_i$, of the forecast error covariance matrix are shown in (e)-(h). Panels (i)-(l) show the expected standard deviation σ of the forecast error for the 12-day forecasts averaged over the same cycles based on the leading 30 EOFs, $\boldsymbol{\psi}_i$, of the forecast error covariance matrix.

Therefore, associated with each EOF $\boldsymbol{\psi}_i$, there is a unique Hessian singular vector that, over the forecast interval, evolves into the EOF. SMA demonstrated that for EOFs like those shown in Fig. 6, the evolution of the Hessian singular vectors proceeds via an *upscale* transfer of energy, which means that the forecast errors move to larger scales over time. To illustrate, Fig. 8 shows the SST structure of the leading Hessian singular vector and associated EOF for a representative cycle, and clearly displays the upscale transfer of energy in the forecast error. SMA also demonstrated that Hessian singular vectors, like that in Fig. 8a, typically grow more rapidly than the most unstable eigenmodes of $\boldsymbol{M}_{\boldsymbol{f}}(0,t)$, explored in section 6b, indicating that the upscale transfer of energy is linked to the interference of the non-normal eigenmodes of the underlying time-evolving circulation which plays an essential role in forecast error growth.

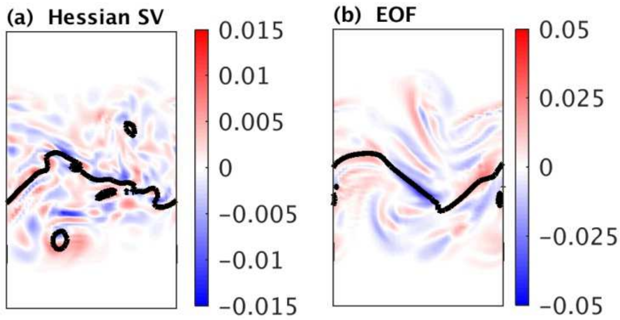

Figure 8: SST for (a) the leading Hessian singular vector and (b) corresponding EOF for a 12-day forecast initialized from the cycle 24 *strong* constraint 4D-Var analysis. The Hessian singular vector was computed using the method of SMA. Also shown is the 9ºC isotherm forecast as an indicator of the position of the temperature front (black line).

b. Finite-time normal modes

The fastest-growing eigenmodes of $\boldsymbol{M}_{\boldsymbol{f}}(0,t)$ play an essential role in error growth as the forecast lead time increases. The eigenvectors of $\boldsymbol{M}_{\boldsymbol{f}}(0,t)$ in (10) are often referred to as Finite-Time Normal Modes (FTNMs). If we denote by $(\nu_i, \boldsymbol{\xi}_i)$ the complex eigenpairs of $\boldsymbol{M}_{\boldsymbol{f}}(0,t)$, then $|\upsilon_i|^2$ is the factor by which *any* measure of the amplitude of FTNM $\boldsymbol{\xi}_i$ changes over the time interval $[0,t]$. Figure 9a shows $|\upsilon_1|^2$ for the leading FTNM $\boldsymbol{\xi}_1$ as a function of forecast lead time for two cycles that reflect the different behavior of the total variance: cycle 9 where total variance first decreases and later increases, and cycle 23 where total variance continually decreases with increasing lead time (*cf.*, Figs. 3b and 3c). Error growth is possible in both cases since $|\upsilon_1|^2 > 1$ in Fig. 9a. For cycle 9, the growth factor $|\upsilon_1|^2$ generally increases with lead time, while for cycle 23 $|\upsilon_1|^2$ changes very little with lead time. For an unstable circulation, we would usually expect $|\upsilon_1|^2$ to increase steadily with forecast lead time, and for the autonomous case $|\upsilon_1|^2$ would increase exponentially with t. Therefore, a more useful measure of FTNM growth is $|\upsilon_1|^2/t$, an indicator of the average growth rate. Figure 9b shows $|\upsilon_1|^2/t$ versus lead time t for the same two forecast cycles. During forecast cycle 9, the average growth rate of $\boldsymbol{\xi}_1$ decreases during the first 10 days, remains low until around t =20 days, and increases again for longer lead times. This behavior is similar to that of the forecast error variance in Figs. 3b and 3c during the same cycle. Similarly, the average growth rate of $\boldsymbol{\xi}_1$ for forecast cycle 23 decreases with lead time t, mirroring the behavior of the forecast error variance during this cycle in Figs. 3b and 3c.

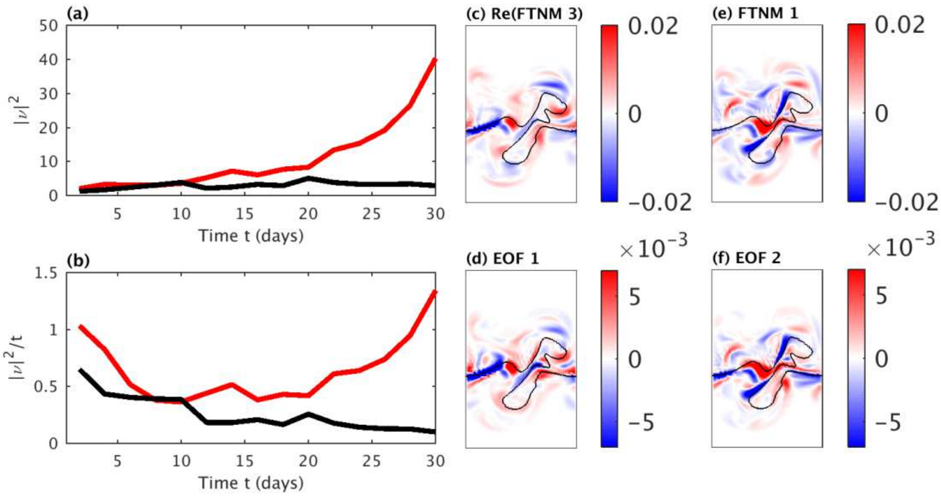

Figure 9: (a) The growth factor $|\upsilon_1|^2$of the leading FTNM versus forecast lead time t for forecast cycles 9 (red) and 23 (black). (b) The average growth rate $|\upsilon_1|^2/t$ of the leading FTNM versus forecast lead time t for forecast cycles 9 (red) and 23 (black). (c) The SST structure of the real component of FTNM $\boldsymbol{\xi}_3$ for a 30-day forecast of cycle 9. (d) The SST of the leading EOF $\boldsymbol{\psi}_1$ for a 30-day forecast of cycle 9. The SST of (e) FTNM $\boldsymbol{\xi}_1$, which is purely real and (f) EOF $\boldsymbol{\psi}_2$ for a 30-day forecast of cycle 9. The FTNM and EOF amplitudes differ because they are normalized differently. The 9ºC isotherm forecast is also shown as an indicator of the position of the temperature front (black line).

The structure of the EOFs for long forecast leads times is also controlled by the most unstable FTNMs. To illustrate this, suppose for a moment that forecast error $\boldsymbol{\varepsilon}$ is due solely to the leading unstable FTNM. In general, the eigenvectors of $\boldsymbol{M_f}(0,t)$ will form complex conjugate pairs. If the leading eigenmode is complex, it must be combined with its complex conjugate to yield a real perturbation, in which case $\boldsymbol{\varepsilon}(t) = c(t)\boldsymbol{\xi}_1 + c^*(t)\boldsymbol{\xi}_1^*$ in this example, where $c(t)$ is the complex amplitude. If we assume that the real and imaginary components of $c(t)$ are Gaussian random variables with zero mean and variance σ^2, then the forecast error covariance is given by $E\{\boldsymbol{\varepsilon}(t)\boldsymbol{\varepsilon}^T(t)\} = 4\sigma^2(Re(\boldsymbol{\xi}_1)Re(\boldsymbol{\xi}_1)^T + Im(\boldsymbol{\xi}_1)Im(\boldsymbol{\xi}_1)^T)$. This will be, at most, a rank 2 matrix, and the two EOFs will be given by linear combinations of the real and imaginary components of $\boldsymbol{\xi}_1$. In the general case, several of the leading FTNMs will contribute to $\boldsymbol{\varepsilon}$, and the EOFs will reflect the structure of several modes. To illustrate, Figs. 9c and 9d show the SST structure of the real component of FTNM $\boldsymbol{\xi}_3$ and EOF $\boldsymbol{\psi}_1$, respectively for the 30-day forecast initialized from the 4D-Var analysis of cycle 10. In this case, there are several growing FTNMs with similar growth factors ($|\upsilon|^2$ is 40, 31, 12, and 6 for the leading four FTNMs), and the EOF is clearly controlled by $\boldsymbol{\xi}_3$ in this case. Figures 9e and 9f, on the other hand, show the SST of $\boldsymbol{\xi}_1$, and EOF $\boldsymbol{\psi}_2$, which are very similar. For shorter forecast lead times, the link between the leading EOF structures and the most unstable FTNMs is less pronounced (not shown).

The emergence of coherent and persistent error structures associated with the most unstable FTNMs is also reflected in the properties of the auto-covariance matrix of the forecast errors $\boldsymbol{UF}(t,t')\boldsymbol{U}^T = E\{\boldsymbol{U\varepsilon}(t)\boldsymbol{\varepsilon}^T(\boldsymbol{t}')\boldsymbol{U}^T\}$. Using again Jacobi's formula, the cyclic properties of the trace, and (14) it follows that $d\left[\ln\left(det\big(\boldsymbol{F}(t,t')\big)\right)\right]/dt = d\left[\ln\left(det\big(\boldsymbol{F}(t)\boldsymbol{F}(t')\big)^{1/2}\right)\right]/dt$ where

$\boldsymbol{F}(t)$ and $\boldsymbol{F}(t')$ are the zero-lag forecast error covariance matrices at time t and t' respectively. Figure 4 includes time series of $d\left[\ln\left(det\left(\boldsymbol{F}(30,t')\right)\right)\right]/dt$ versus t' for 30-day forecasts during cycles 2 and 26. While the volume of the hyper-ellipsoid $det(\boldsymbol{UF}(30,t')\boldsymbol{U}^T)^{1/2}$ behaves qualitatively like that associated with $\boldsymbol{F}(t) = \boldsymbol{F}(t,t)$ in Fig. 3a (not shown), Fig. 4 reveals that the rate of change of volume increases as the covariance lag $(t - t')$ decreases. Therefore, the coherence between the spatial structures of the forecast errors $\boldsymbol{\varepsilon}(t)$ at different lead times is increasing, which is consistent with the emergence of the most unstable FTNMs.

c. Non-linearity

The dynamics of perturbation growth in shear flows associated with normal modes, and the interference of modes is a well-understood process (*e.g.*, Pedlosky, 1976; Farrell and Ioannou, 1996), and perturbations can grow by extracting energy from the underlying time-evolving circulation via the familiar processes of baroclinic and barotropic energy conversion. This is an appropriate and convenient framework for the evolution of forecast errors considered here since, recall, we are using energy as the common currency for the various components of the state-vector to compute the error covariance matrix. In general, the same processes that control the formation of the eddies and meanders in Model T are also responsible for the growth of forecast errors in Model F.

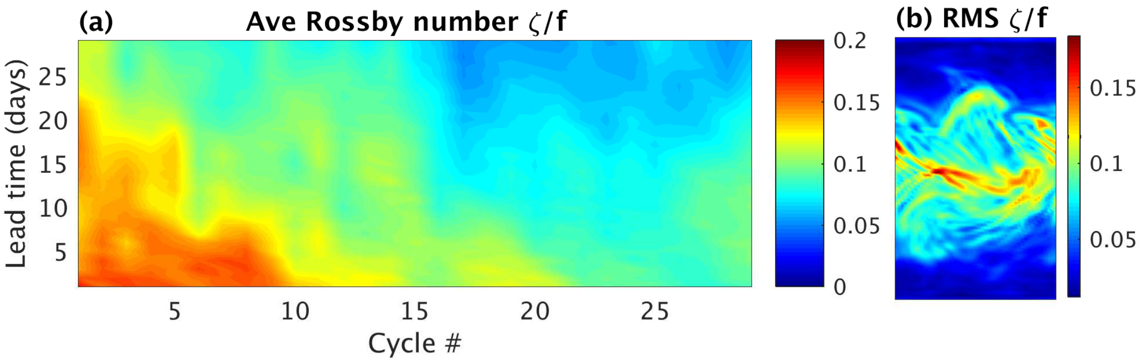

Figure 10: (a) The mean local Rossby number $\overline{\zeta/|f|}$ at the surface computed from daily averaged forecasts versus forecast lead time for each analysis-forecast cycle. (b) The root-mean-square local Rossby number for 12-day forecasts averaged over cycles 21-30.

With this in mind, the evolution and properties of the forecast errors will depend on the degree of non-linearity of the underlying reference forecast $\boldsymbol{x}^f$ (*cf.*, Fig. 1) since the processes involved act as the source of energy in the tangent linear model. As a measure of the importance of non-linearity, Fig. 10a shows the mean local Rossby number, denoted $\overline{\zeta/|f|}$, averaged over a 400 km wide zonal strip centered in the middle of the model domain (*i.e.*, where the circulation variability is most energetic – see Fig. 2), and computed from the daily averaged surface flow. Figure 10a indicates that non-linearity has the greatest influence on the circulation during the first 10-15 analysis-forecast cycles. While $\overline{\zeta/|f|}$ reaches modest values ~0.2 during these cycles, this nonetheless represents a significant departure from the linear quasi-geostrophic regime. Indeed, maximum instantaneous *in situ* values of $\zeta/|f|$ can be significantly larger and are O(1) in some cases (not shown). During this phase of the experiment, Figs. 2a and 2b indicate that the growth of a zonal wavenumber-2 instability dominates the Model T circulation. Beyond cycle 15, the mean Rossby number is generally at or below ~0.1 when maximum instantaneous *in situ* values of $\zeta/|f|$ are also lower (not shown). For these analysis-forecast cycles, the Model T circulation is dominated by the evolution of a zonal wavenumber-1 instability (*cf.,* Figs. 2c and 2d). Despite the difference in resolution, Model F mimics the temporal evolution of $\overline{\zeta/|f|}$ for Model T, although, as expected, the Rossby number is larger in Model T (not shown).

Figure 10a indicates that the elevated Rossby numbers during the first 10-15 cycles occur at short forecast lead times, and then taper off, suggesting that there will be significant sources of perturbation energy (*i.e.*, forecast error variance) during the early phase of these forecasts. The subsequent increase in total forecast error variance $tr(\boldsymbol{UF}(t)\boldsymbol{U}^T)$ (*i.e.*, energy) at longer lead times during these analysis-forecast cycles, as revealed by Fig. 3b, suggests that the stretching of the hyper-ellipsoid (and the increase in the associated hyper-ellipsoid volume in a few cases), is due to the sustained growth of perturbations that are excited early in the forecast period and that significantly project onto the fastest growing FTNMs, that eventually emerge as coherent patterns of error. As shown by SMA, some of this growth is likely to be enhanced by non-normal interference of the modes and an upscale transfer of forecast error variance, as evidenced by the behavior of the Hessian singular vectors discussed in section 6a.

Figure 10b shows the spatial variations in the root mean square of $\zeta/|f|$ for 12-day forecasts initialized from 4D-Var cycles 21-30. The regions of elevated Rossby number in Fig. 10b correspond closely with the "hot spots" of high expected forecast error shown in Figs. 7i-l. The resemblance is striking for SSH (Fig. 7i) and SST (Fig. 7j) and confirms the role of non-linearity in controlling local forecast error growth and forecast skill.

7. Summary and Conclusions

This paper focuses on the properties of the expected analysis and forecast error covariance matrices that result from 4D-Var data assimilation analyses of the mesoscale circulation environment that develops in the presence of a baroclinically unstable oceanic temperature front. Given the ubiquitous nature of this process in the ocean, the findings of this work should be widely applicable. A novel aspect of this study lies in the methodology used. Specifically, the tangent linearization of the full data assimilation system and its adjoint were used to compute an explicit operator for the expected error covariance. This has considerable appeal over other methods, such as ensemble approaches, that are commonly used to estimate analysis and forecast error covariance matrices, since the covariance operator is free of the limitations associated with ensemble size, localization methods, etc. The downside of our approach, however, is the considerable computational expense involved. Nevertheless, the technique can be applied to modestly-sized data assimilation problems of significant theoretical interest, such as the case considered here. A significant advantage of our method over that computed from an ensemble is that, as noted in section 2, equations (7) and (8) provide an *explicit* operator for the analysis error covariance matrix (and equation (9) for the forecast error covariance matrix) which can be used to interrogate intrinsic properties of the system (as here) using established methods and results of linear algebra.

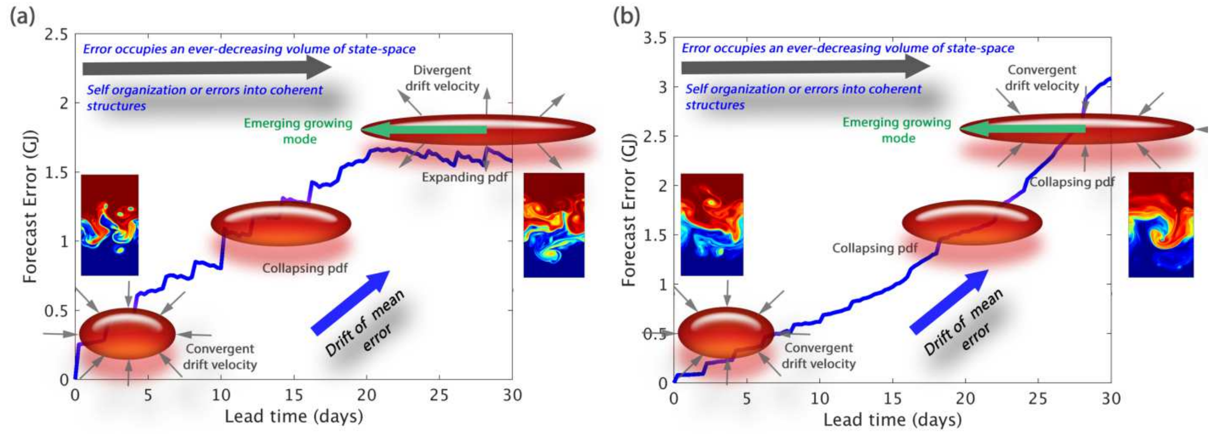

Figure 11: A schematic summarizing the evolution of the forecast error covariance during the development of the temperature front adjustment during (a) cycle 6, and (b) cycle 30. For each cycle, a time series of the forecast error energy is shown (blue line) computed from the 4D-Var analyses on the same forecast day. The red ellipsoids show a schematic representation of the evolution of the forecast error covariance hyper-ellipsoids through time. The grey short grey arrows indicate whether the *drift velocity* is convergent or divergent. The blue arrow shows the tendency of the drift of the mean of the pdf, while the green arrow indicates the emergence of the fastest-growing FTNMs that stretch the hyper-ellipsoid in preferred directions. Also shown in the inset panels is the SST of the true circulation at initial and final forecast time. During cycle 6, the flow is characterized by a mature zonal wavenumber-2 instability that undergoes decay during the subsequent 30-day forecast period. Conversely, during cycle 30, a zonal wavenumber-1 instability develops that forms a sizeable roll-up meander.

Our general findings are summarized in Fig. 11, which shows a schematic of the behavior of the forecast error covariance matrix for two representative forecast cycles that depict the two different scenarios identified. These two scenarios are characterized by the development of baroclinically unstable waves with a wavelength corresponding to one channel width (zonal wavenumber-1) and one half-channel width (zonal wavenumber-2). SMA computed the growth rates of these two waves and found that the zonal wavenumber-2 instability has a faster growth rate and so it emerges first within the model simulations.

(i) *Scenario 1*

The first scenario corresponds to the period spanned by the first half-a-dozen or so analysis-forecast cycles. The observed circulation environment is characterized by a fully developed zonal wavenumber-2 instability that subsequently decays during the time interval spanned by the ensuing 30-day forecasts. The behavior of the forecast error covariance during this period is summarized in Fig. 11a using cycle 6 as a representative example. Figure 11a shows a time series of the forecast error energy for this cycle as a function of forecast lead time and computed from the difference between the forecast state and the 4D-Var analysis on the same day. The initial and final time SST for the forecast are also shown in Fig. 11a and reveal the decay of the zonal wavenumber-2 instability. During the forecast, the forecast error grows out to a lead time ~20 days, after which time it levels off. During the error growth phase of this forecast cycle, the volume of the hyper-ellipsoid associated with the forecast error covariance matrix decreases (*cf.*, Fig. 3a), which is associated with a convergent *drift velocity* in the Liouville equation that describes the time evolution of the forecast error pdf (*cf.*, Fig. 4a for cycle 2 which displays similar behavior to cycle 6 shown here). At the same time, the total forecast error variance decreases (*cf.*,

Fig. 3b), and the hyper-ellipsoid stretches along the directions described by the leading EOFs, as described in section 5a. This initial phase of forecast error growth is illustrated schematically in Fig. 11a by the red ellipsoids. During the period beyond forecast day 20, when the forecast error asymptotes to a more constant level, the pdf *drift velocity* becomes divergent (*cf.,* Fig. 4a), and the forecast error covariance hyper-ellipsoid begins to expand (*cf.,* Fig. 3a). At the same time, the total forecast error variance increases (*cf.,* Fig. 3b) and the hyper-ellipsoid is preferentially stretched along the directions associated with the fastest-growing FTNMs. This phase of the forecast error development is also illustrated in Fig. 11a.

(ii) *Scenario 2*

The second scenario in the experiments considered here corresponds to the growth and development of the zonal wavenumber-1 instability that follows after the decline of zonal wavenumber-2. The behavior of the forecast error covariance during this period is summarized in Fig. 11b using cycle 30 as a representative example. The forecast error energy, in this case, increases during the entire forecast cycle, as shown in Fig. 11b. The initial and final time SST for the forecast are also shown in Fig. 11b and reveal the emergence of the wavenumber-1 instability. During the entire forecast cycle, in this case, the volume of the forecast error covariance hyper-ellipsoid decreases (*cf.*, Fig. 3a) and the pdf *drift velocity* in the Liouville equation remains convergent (*cf.*, Fig. 4b for cycle 26 which displays similar behavior to cycle 30 shown here). The total forecast error variance at first decreases until around forecast day 18, and then slowly increases (*cf.,* Fig. 3b). Throughout the forecast, the hyper-ellipsoid stretches along the directions described by the leading EOFs as the fastest-growing FTNM begin to emerge, as illustrated schematically in Fig. 11b by the red ellipsoids.

The temporal behavior of hyper-ellipsoid volume and total error variance can be further appreciated by appealing to a simple example. Consider the 2×2 covariance matrix $\boldsymbol{C}$ with eigenvectors λ_1 and λ_2. The total variance is given by $(\lambda_1 + \lambda_2)$ and the determinant by $\lambda_1\lambda_2$. In cases where the variations in $(\lambda_1 + \lambda_2)$ and $\lambda_1\lambda_2$ are positively correlated, there is no significant restriction on the relative amplitude of λ_1 and λ_2. Conversely, during times when $(\lambda_1 + \lambda_2)$ increases and $\lambda_1\lambda_2$ decreases, there must be a disparity in the amplitude of the eigenvalues. Therefore, considerable stretching of the error ellipse associated with $\boldsymbol{C}$ will occur along one axis. The same principle applies in higher dimensions and illustrates the geometric factors that control the variations in the topology of the hyper-ellipsoid associated with the variations of the determinant and trace of the forecast error covariances in Fig. 3. The close connection between the EOFs of forecast error and the FTNMs also suggests a disparity in the spectrum of FTNM growth rates, which in turn favors non-normal forecast error growth due to the interference of the FTNMs (Farrell and Ioannou, 1996). Indeed, SMA confirmed that non-normal growth occurs in this same system, leading to up-scale energy transfer in the forecast errors, as the leading EOFS and FTNMs emerge (*cf.,* Fig. 8). Therefore, in general, forecast errors at small scales are liable to self-organize into larger-scale coherent structures.

The difference in the temporal evolution of the forecast error energy between the two cases considered in Fig. 11 deserves some further comment. The leveling off of the forecast error energy in Fig. 11a may perhaps be associated with non-linear saturation of the forecast error amplitude. If that is the case, then the forecast error covariance $\boldsymbol{UFU}^T$ during this phase of the forecast would be largely time-invariant (*i.e.,* stationary error statistics), in which case the determinant and trace would remain constant in time. This is at odds, though with Fig. 3. However, equation (13), which describes the time evolution of the forecast error covariance, is predicated on the tangent linear assumption. In this case, the behavior of the total forecast error variance and hyper-ellipsoid volume beyond forecast day 20 in Fig. 3 could perhaps be a symptom of linearization errors. Indeed, the analysis in Fig. 9b does indicate that during the period under consideration, the average growth rate of the leading FTNM receives a boost around forecast day 20. Equation (14) provides additional evidence in that the eigenspectrum of the tangent linear operator $\boldsymbol{\Phi_f}(t)$ comprises complex conjugate pairs of eigenvectors and eigenvalues. The real part of the eigenvalues represents the *instantaneous* growth rate of forecast errors associated with these eigenvectors. Thus $tr(\boldsymbol{\Phi_f})$ equals twice the sum of the instantaneous growth rates of the *instantaneous* eigenvectors. Therefore, the change in sign of $tr(\boldsymbol{\Phi_f})$ in Fig. 4a is indicative of a switch from predominantly decaying *instantaneous* modes of $\boldsymbol{\Phi_f}$ to predominantly growing modes. However, for the non-autonomous cases considered here, there is no clear relationship between the *instantaneous* eigenvectors of $\boldsymbol{\Phi_f}(t)$ and the FTNMs of $\boldsymbol{M_f}(0,t)$. Furthermore, while Fig. 11a shows what we believe to be the behavior during a representative example of scenario 1, other forecast cycles during this period exhibit a decline in forecast error energy at a lead time beyond 20-days (not shown), which is *inconsistent* with non-linear saturation of error amplitude. Besides, it is by no means clear why the forecast error energy during scenario 2 would not saturate over the same forecast lead time, if this is indeed the explanation for the behavior during scenario 1. Further analysis of these issues and behaviors is clearly warranted.

There are some critical limitations of the present study that should be mentioned here. First, no attempt was made to account for model error in calculating the expected analysis and forecast error covariances. Model error is an unavoidable facet of all real forecast systems, so including its influence in the approach presented here represents an important next step. Indeed, the Fokker-Planck equation (12) indicates that the addition of the *diffusion* term would introduce additional and important influences on the forecast error pdf. Nonetheless, Fig. 7 shows that even when model errors are not accounted for, the expected forecast error covariances can still faithfully describe actual error growth and predictability. Caution should be exercised here since, even though the “forecast model” employed in this study is imperfect relative to the observed model, the paternal twin approach adopted in our experiments is unlikely to mimic actual model errors truly. A second limitation of our study is the absence of surface forcing. As discussed in section 2, surface forcing can play an important role in frontogenesis and frontolysis. The inclusion of forcing and the attendant uncertainties in our experiments would undoubtedly increase the diversity of possible ocean forecast states and enhance the forecast error covariance. Finally, while the time scales in Fig. 11 refer to the experiments presented in this paper, the very general nature of the dynamical processes at work in the circulation considered here suggest that Fig. 11 may apply more broadly across the range of scales that support the formation and decay of baroclinically unstable fronts. While we can offer no specific guidance on how our findings may apply more generally across different space- and time-scales (*i.e.*, mesoscale or sub-mesoscale), scaling analysis may shed some light on this, and would be a fascinating topic for further research.

As noted earlier, our approach is computationally demanding. The computational burden required for each calculation depends on the computational resources available, so it is perhaps useful to report the computation time required in terms of the time taken to run a single outer-loop 4D-Var iteration on the computer system available. With this in mind, let t_a represent the CPU time required to perform a single outer-loop of 4D-Var. The expected analysis error covariance matrix $\boldsymbol{A}_n$ given by (7) involves evaluations of the tangent linearization of the 4D-Var algorithm, $\partial\mathcal{K}/\partial\boldsymbol{d}$, and its adjoint $(\partial\mathcal{K}/\partial\boldsymbol{d})^T$, for each outer-loop. The CPU requirements of each integration of $\partial\mathcal{K}/\partial\boldsymbol{d}$ and $(\partial\mathcal{K}/\partial\boldsymbol{d})^T$ is ~t_a. Therefore, for an arbitrary vector $\boldsymbol{u}$, a single matrix-vector product $\boldsymbol{A}_n\boldsymbol{u}$ requires a CPU time $\sim\left(2n+\sum_{j=1}^{n} j\right)t_a$ where n is the number of outer-loops. The cost of a matrix-vector product of $\boldsymbol{F}_n(t)\boldsymbol{u}$ based on (10) is comparable, since the additional integrations of the tangent linear and adjoint models does not add significantly to the computational cost. For the case $n=1$ in all of the examples considered here, a single matrix-vector product $\boldsymbol{Au}$ or $\boldsymbol{F}(t)\boldsymbol{u}$ is ~3 times the cost of a single 4D-Var calculation. The trace and determinant calculations of section 4 using the Bai *et al.* (1996) approach described in appendix C are the most-costly calculations presented in this study. Each data point in Fig. 4a is based on a Monte Carlo of 900 separate evaluations of $\boldsymbol{Au}$ or $\boldsymbol{F}(t)\boldsymbol{u}$ which requires $\sim 2700t_a$, although the same Monte Carlo calculation can be used to estimate the trace associated with any $f(\boldsymbol{A})$ and $f\left(\boldsymbol{F}(t)\right)$. Such calculations would clearly be prohibitive for problems with a dimension much larger than considered here which is $O(10^5)$. Conversely, the trace estimate calculations using the approach of Fisher and Courtier (1995) in appendix C are based on 30 separate evaluations of $\boldsymbol{Au}$ or $\boldsymbol{F}(t)\boldsymbol{u}$ which require $\sim 90t_a$ so are much more tractable, even for larger problems. The CPU time required to compute the EOF calculations of section 5 depends on the number of leading members of the eigenspectrum are desired. As a rule of thumb, computation of reliable estimates of the *N* leading EOFs require ~2*N* evaluations of $\boldsymbol{Au}$ or $\boldsymbol{F}(t)\boldsymbol{u}$ and $\sim 6Nt_a$.

This study represents an intersection between a state-of-the-art ocean analysis-forecast system and the abstract ideas about forecast error development exposed by linear algebra. While our approach is very computationally demanding, computer power continues to increase. Thus, it is conceivable that such calculations could be performed on larger, more realistic systems in the near future. Indeed, when the ROMS tangent linear and adjoint models were first developed almost two decades ago (Moore *et al*. 2004), some of the calculations presented here would not have been possible with the computing facilities available to us at that time. There is potentially a wealth of additional information and a deeper understanding of ocean forecast system behavior that could be mined using the approaches described here. Therefore, we should not feel intimidated by the dimension of the everyday forecast problems at hand.

Acknowledgements: This work was supported by a Basic Research Challenge grant from the Office of Naval Research (N00014-10-1-0476) and by Southwest Universities Research Association (SURA) as part of the Coastal Ocean Modeling Testbed (COMT, NA13NOS0120139) project. We are grateful to the four anonymous reviewers for their positive and helpful comments, and to one of the reviewers for pointing out that sparse grid methods could possibly be used to reduce the computational cost of the trace and determinant calculations.

APPENDIX A

Energy scaling for the error covariance

If we denote by $\boldsymbol{\varepsilon}$ the vector of grid-point values of errors in free surface elevation, ε_ζ, the horizontal components of velocity, ε_u and ε_v, and temperature, ε_T, then following Smith *et al.* (2015) $\boldsymbol{U}$ is defined such that $\mathcal{E} = \boldsymbol{\varepsilon}^T \boldsymbol{U}^T \boldsymbol{U} \boldsymbol{\varepsilon}$ is the total *perturbation* energy of the errors given by:

$$\mathcal{E} = \frac{g\rho_0}{2} \sum_{ij} \left(\varepsilon_\zeta\right)_{ij}^2 dA_{ij} + \frac{\rho_0}{2} \sum_{ijk} \left\{(\varepsilon_u)_{ijk}^2 + (\varepsilon_v)_{ijk}^2\right\} h_{ijk} dA_{ij} + \frac{\rho_0}{2} \left(\frac{\alpha g}{N_0}\right)^2 \sum_{ijk} (\varepsilon_T)_{ij}^2 h_{ijk} dA_{ij} \quad \text{(A1)}.$$

where, g is the acceleration due to gravity, $\rho_0 = 1025$ kg m^{-3} is the mean ocean density, $\alpha = 1.6 \times 10^{-4}$ K^{-1} is the thermal expansion coefficient of sea water, and $N_0 = 3.2 \times 10^{-3}$s is a representative value of the Brunt-Väisälä frequency. The summations are performed over all ROMS grid cells in the horizontal (ij) and in the vertical (k) where dA_{ij} is the horizontal grid cell area and h_{ijk} is the grid cell thickness. The first term in (A1) represents the perturbation potential energy associated with errors in surface elevation, the second term is the perturbation kinetic energy due to errors in the horizontal velocity, and the last term is the available perturbation potential energy associated with errors in the density. Recall that only temperature is included in the ROMS configuration used here, and for convenience we use have assumed a linear equation of state for the density errors $\varepsilon_\rho = -\rho_0 \alpha \varepsilon_T$. In addition, since the grid used here has uniform grid-spacing dA, the error norm used in all calculations was actually $\mathcal{E}/dA$, the energy per unit area. Therefore, $\boldsymbol{U}$ is a diagonal matrix with elements given by $(g\rho_0/2)^{1/2}$, $\left(g\rho_0 h_{ijk}/2\right)^{1/2}$, and $\left(\rho_0 h_{ijk}/2\right)^{1/2}(\alpha g/N_0)$ as appropriate.

APPENDIX B

Covariance from perturbed 4D-Var analyses

As described by Gürol *et al.* (2014), the inverse preconditioned stabilized representer matrix $(\boldsymbol{R}^{-1}\boldsymbol{H}\boldsymbol{B}\boldsymbol{H}^T + \boldsymbol{I})^{-1}$ in (2) is factorized in the ROMS dual 4D-Var system using the Lanczos formulation of the **B**-restricted preconditioned conjugate gradient method of Gratton and Tshimanga (2009) according to:

$$(\boldsymbol{R}^{-1}\boldsymbol{H}\boldsymbol{B}\boldsymbol{H}^T + \boldsymbol{I})^{-1} \approx \boldsymbol{V}_m \boldsymbol{T}_m^{-1} \boldsymbol{V}_m^T \boldsymbol{H}\boldsymbol{B}\boldsymbol{H}^T \qquad \text{(B1)}$$

where $\boldsymbol{V}_m$ is the matrix of Lanczos vectors $\boldsymbol{v}_i$ arising from *m* inner-loops, and $\boldsymbol{T}_m = \boldsymbol{V}_m^T \boldsymbol{H}\boldsymbol{B}\boldsymbol{H}^T (\boldsymbol{R}^{-1}\boldsymbol{H}\boldsymbol{B}\boldsymbol{H}^T + \boldsymbol{I}) \boldsymbol{V}_m$ is a symmetric tridiagonal matrix. Each Lanczos vector represents a conjugate gradient descent direction, and the $\boldsymbol{v}_i$ are orthonormal according to $\boldsymbol{V}_m^T \boldsymbol{H}\boldsymbol{B}\boldsymbol{H}^T \boldsymbol{V}_m = \boldsymbol{I}_m$. The Lanczos vectors $\boldsymbol{V}_m$ span a limited subspace of the full control space, and as such, the subspace orthogonal to $\boldsymbol{V}_m$ will not be constrained by 4D-Var.

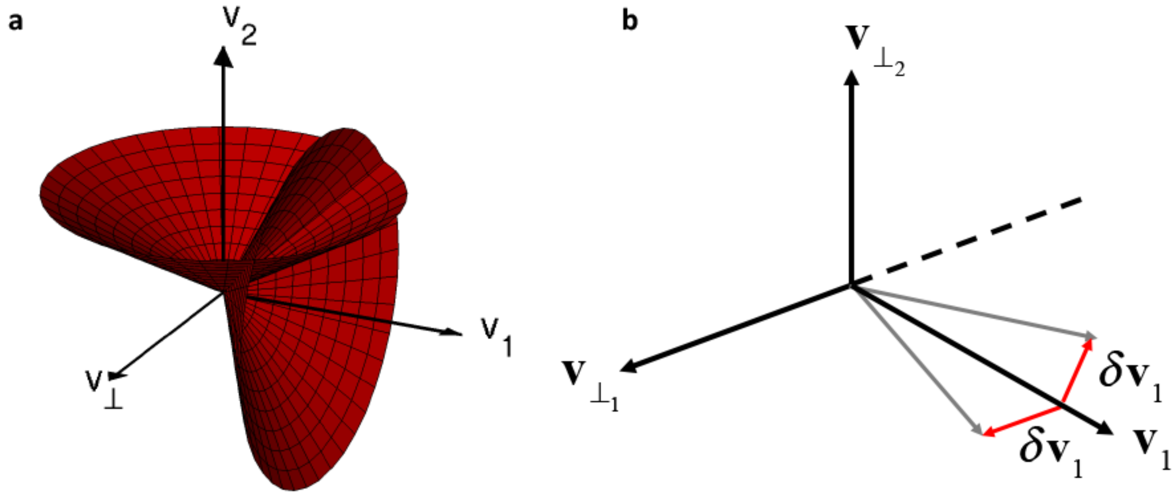

Figure B1: (a) A schematic showing the space spanned by the Lanczos vectors $\boldsymbol{v}_1$ and $\boldsymbol{v}_2$ in the case of two inner-loops, and the subspace $\boldsymbol{v}_\perp$ that is not constrained by 4D-Var. The intersecting red cones (drawn to scale) show the standard deviation of the directions in the perturbed Lanczos vectors arising from perturbations in the observations and background from distributions $N(\mathbf{0},\boldsymbol{R})$ and $N(\mathbf{0},\boldsymbol{B})$ respectively. (b) A schematic showing the space spanned by the Lanczos vector $\boldsymbol{v}_1$ in the case of a single inner-loop. In this case, the space that is not constrained by 4D-Var is divided into $\boldsymbol{v}_{\perp_1}$ and $\boldsymbol{v}_{\perp_2}$. The Lanczos vector perturbations $\delta\boldsymbol{v}_1$ in this case project onto the subspace $\boldsymbol{v}_{\perp_1}$but not $\boldsymbol{v}_{\perp_2}$.

As described in section 2b, the expected analysis error covariance matrix can be derived by considering an ensemble of 4D-Var analyses, where each ensemble member is computed by perturbing the background $\boldsymbol{x}^b$ and the observations $\boldsymbol{y}^o$ with perturbations drawn from Gaussian distributions $N(\mathbf{0},\boldsymbol{B})$ and $N(\mathbf{0},\boldsymbol{R})$ respectively. Each set of perturbations leads to perturbations $\delta\boldsymbol{V}_m$ in the Lanczos vectors. While the perturbed Lanczos vectors will span only a small subspace of the full control space, each resulting $\boldsymbol{V}_m$ defined by the ensemble will span a different set of subspaces. Therefore, the resulting ensemble of 4D-Var analyses will span a larger subspace than any single analysis. This is illustrated schematically in Fig. B1a which shows the case for $m = 2$. Figure B1a shows the directions of the Lanczos vectors $\boldsymbol{v}_1$ and $\boldsymbol{v}_2$ for the original unperturbed 4D-Var analysis. The subspace that is *unconstrained* by the 2 inner-loops is denoted as $\boldsymbol{v}_\perp$. Also shown in Fig. B1a, drawn to scale, is the standard deviation of the range of the perturbed Lanczos vectors that result from an infinite ensemble. Clearly, some of the perturbed Lanczos vectors will project significantly into $\boldsymbol{v}_\perp$, thus expanding the subspace spanned by 4D-Var. However, there will still be parts of the control space that are unconstrained by 4D-Var. For example, consider Fig. B1b, which shows the case of $m = 1$ for illustrative purposes. In this case, the subspace unconstrained by 4D-Var has been divided into two denoted $\boldsymbol{v}_{\perp_1}$ and $\boldsymbol{v}_{\perp_2}$. As shown in Fig. B1b, the perturbed Lanczos vectors provide information about $\boldsymbol{v}_{\perp_1}$, while $\boldsymbol{v}_{\perp_2}$remains unconstrained.

APPENDIX C

Iterative methods for estimating the determinant and trace of a matrix

For the large dimension problem considered here (~10^5), it is not practical to explicitly compute the analysis and forecast error covariance matrices. Therefore, properties such as the determinant, trace, and eigenspectrum must be calculated using iterative approaches. Two approaches have been employed in this study. The first is based on Bai *et al.* (1996; hereafter, BFG) and is used to estimate the determinant and trace of a matrix. Since it is based on the Lanczos algorithm, it can also be used to reliably compute the leading members of the eigenspectrum. The second approach is based on Fisher and Courtier (1995; hereafter, FC). While this latter approach is more straightforward to implement than BFG, it only yields an estimate of the matrix trace. A comparison of the trace estimates obtained from the two independent approaches provides a check on the efficacy of the results.

a The BFG approach

The diagonal elements of the real square matrix $\boldsymbol{C}$ can be expressed as the inner-product $C_{ii} = \boldsymbol{e}_i^T \boldsymbol{C} \boldsymbol{e}_i$ where $\boldsymbol{e}_i$ is i^{th} column of the identity matrix. Furthermore, if $f(\boldsymbol{C}) = f(\lambda)$ is a smooth function of the eigenspectrum λ of $\boldsymbol{C}$, then $\boldsymbol{e}_i^T f(\lambda) \boldsymbol{e}_i$ yields the i^{th} diagonal element of the associated matrix. In BFG, the trace of $f(\boldsymbol{C}) = f(\lambda)$ is replaced by an integral, which can then be estimated using different Gauss-quadrature rules. Specifically, BFG have developed a Monte Carlo approach to estimate lower and upper bounds on the inner-product $I = \boldsymbol{u}^T f(\boldsymbol{C}) \boldsymbol{u}$. Then, if $f(\lambda) = \lambda$, the inner-product I will yield upper and lower bounds on $tr(\boldsymbol{C})$. Similarly, $f(\lambda) = \lambda^{-1}$ can provide bounds on $tr(\boldsymbol{C}^{-1})$, and $f(\lambda) = \ln \lambda$ will yield bounds on $tr(\ln \boldsymbol{C}) = \ln\big(det(\boldsymbol{C})\big)$. An ensemble of estimates of I_j are computed by using different vectors for $\boldsymbol{u}_j$ with elements of either +1 or -1 that are chosen at random with equal probability (*i.e.* "Algorithm 2" of BFG). For each choice of random vector $\boldsymbol{u}_j$, the Lanczos algorithm (Golub and van Loan, 1989) is used to estimate the eigenvalues λ_i. Note, that this application of the Lanczos algorithm is distinct and separate from that used in the 4D-Var algorithm described in appendix B. All that is required is a routine that evaluates the matrix-vector product $\boldsymbol{C}\boldsymbol{u}_j$. The inner-product estimate resulting from Gauss-quadrature is then given by $I_j = \sum_{k=1}^{M} \omega_k^2 \lambda_k$ where the weights ω_k^2 are derived from the Lanczos algorithm itself. By applying different rules to the resulting Gauss-quadrature of the function $f(\lambda)$, estimates on the upper $\big(U_j\big)$ and lower $\big(L_j\big)$ bounds for each I_j can be computed. Using a Monte Carlo sample of size p, the upper and lower bounds of $f(\lambda)$ can be calculated as $1/p \sum_j^p U_j$ and $1/p \sum_j^p L_j$, respectively. In the calculations presented in section 4, $M = 90$ and $p = 10$ ($p = 20$ for 30-day forecast lead times), and the matrix-vector product $\boldsymbol{C}\boldsymbol{u}_j$ for each sample member is computed using equation (8) or (10), as appropriate, by employing the tangent linear and adjoint of the ROMS 4D-Var system.

b The FC approach

The method employed by FC is also based on a Monte Carlo approach to estimate $tr(\boldsymbol{C})$. In this case, $tr(\boldsymbol{C}) \approx 1/q \sum_j^q \boldsymbol{u}_j^T \boldsymbol{C} \boldsymbol{u}_j$ where q is the sample size, and the elements of $\boldsymbol{u}$ are normally distributed as $N(0,1)$. While the practical implementation of this approach is more straightforward than that of BFG, it is limited to estimates of $tr(\boldsymbol{C})$. The expected percentage error in the trace estimate is given by $100/(2q)^{1/2}$. In the calculations of section 4, a sample size $q = 30$ was used, which yields an expected error a little shy of 13%. To reduce the error to, say, 1% would require a sample size of 5000, which is impractical.

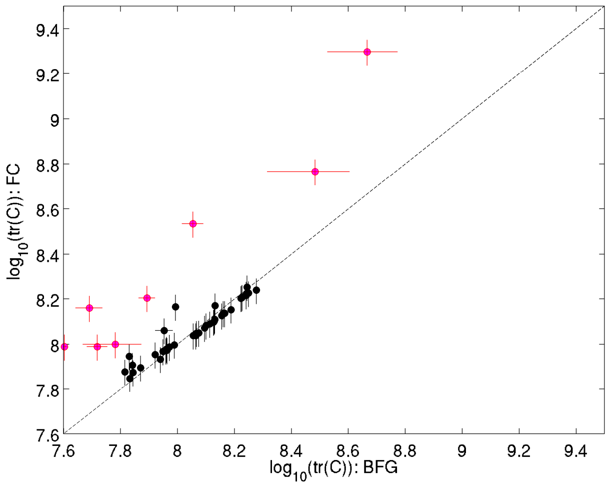

Figure C1: A scatter plot of BFG estimates (abscissa) versus FC estimates (ordinate) of $\log_{10}\left(tr(\boldsymbol{UAU}^T)\right)$ for the analysis error covariance matrices using (8) and (9), and $\log_{10}\left(tr(\boldsymbol{UF}(t)\boldsymbol{U}^T)\right)$ for the forecast error covariance matrices using (10) at various lead times, t. The upper and lower bounds for the BFG estimates and uncertainties for the FC estimates are indicated for each point. The points in red are for a 30-day lead time. For reference, the 1:1 line is also shown (black dashed line).

A comparison of the BFG and FC estimates of $tr(\boldsymbol{UAU}^T)$ for the expected analysis error covariance matrices $\boldsymbol{A}(-\tau)$ (equation (8)) and $\boldsymbol{A}(0)$ (equation (9)), and for the expected forecast error covariance matrices $tr(\boldsymbol{UF}(t)\boldsymbol{U}^T)$ (equation 10) at various lead times t are shown in Fig. C1. In all cases, $\boldsymbol{U}$ defines the energy norm (see appendix A). For $t < 30$, the two methods yield consistent estimates that fall close to the 1:1 line. For $t = 30$, the FC estimates are higher than those of BFG. Despite the disagreement for these longer lead forecasts, Figs. 3b and 3c show that on the whole, the time evolution of the trace estimates yielded by the two approaches is consistent. Therefore, we feel confident that the BFG determinant estimates in Fig. 3a are reliable and that the evolution in time is robust.

References

Anderson, J., 2007: An adaptive covariance inflation error correction algorithm for ensemble filters. *Tellus*, **59A**, 210–224. https://doi.org/10.1111/j.1600-0870.2006.00216.x

Arnold, L., 1998: Random Dynamical Systems. Springer-Verlag, pp586.

Arcucci, R., L. D'Amore, and L. Carracciuolo, 2015: On the problem-decomposition of scalable 4D-var data assimilation models. *IEEE*, 589–594. DOI: 10.1109/HPCSim.2015.7237097

Bai, Z., M. Fahey and G. Golub, 1996: Some large-scale matrix computation problems. *J. Computational and Applied Math.*, **74**, 71-89. https://doi.org/10.1016/0377-0427(96)00018-0

Banerjee, S., B. Carlin, and A. Gelfand, 2004: Hierarchical modeling and analysis for spatial data. *Monographs on Statistics and Applied Probability*, **101**, 2466–2498.

Barker, T.W., 1991: The relationship between spread and forecast error in extended-range forecasts. *J. Climate*, **4**, 733-742. https://doi.org/10.1175/15200442(1991)004<0733:TRBSAF>2.0.CO;2

Barkmeijer, J., M. van Gijzen, and F. Bouttier, 1998: Singular vectors and estimates of the analysis-error covariance metric. *Q. J. R. Meteorol. Soc.*, **124**, 1695–1713. https://doi.org/10.1002/qj.49712454916

Belo-Pereira, M., and L. Berre, 2006: The use of an ensemble approach to study the background error covariances in a global NWP model. *Mon. Wea. Rev.*, **134**, 2466–2498. https://doi.org/10.1175/MWR3189.1

Berre, L., S. Stefaanescu, and M. B. Pereira, 2006: The representation of the analysis effect in three error simulation techniques. *Tellus*, **58A**, 196–209. https://doi.org/10.1111/j.1600-0870.2006.00165.x

Boccaletti, G., R. Ferrari, and B. Fox-Kemper, 2007: Mixed layer instabilities and restratification. *J. Phys. Oceanogr.*, **37**, 2228–2250. https://doi.org/10.1175/JPO3101.1

Buizza, R., and T. Palmer, 1995: The singular-vector structure of the atmospheric global circulation. *J. Atmos. Sci.*, **52**, 1434–1456. https://doi.org/10.1175/1520-0469(1995)052<1434:TSVSOT>2.0.CO;2

Courtier, P., J.-N. Thépaut, and A. Hollingsworth, 1994: A strategy for operational implementation of 4D-Var using an incremental approach. *Q. J. R. Meteorol. Soc.*, **120**, 1367–1388. https://doi.org/10.1002/qj.49712051912

Daley, R., 1991: Atmospheric Data Analysis. Cambridge University Press, 457 pp.

D'Amore, L., R. Arcucci, L. Carracciuolo, and A. Murli, 2014: A scalable and approach to variational data assimilation. *J. Comp. Sci*., **61**, doi:DOI10.1007/s10915-014-9824-2.

Ehrendorfer, M., and J. Tribbia, 1997: Optimal prediction of forecast error covariances through singular vectors. *J. Atmos. Sci*., **39**, 286–313. https://doi.org/10.1175/1520-0469(1997)054<0286:OPOFEC>2.0.CO;2

Epstein, E.S., 1969: Stochastic dynamic prediction. *Tellus*, **21**, 739-759. https://doi.org/10.3402/tellusa.v21i6.10143

Farrell, B.F. and P.J. Ioannou, 1996: Generalized stability theory. Part I: Autonomous operators. *J. Atmos. Sci.*, **53**, 2025-2040. https://doi.org/10.1175/1520-0469(1996)053<2025:GSTPIA>2.0.CO;2

Fisher,M., and P. Courtier, 1995: Estimating the covariance matrices of analysis and forecast error in variational data assimilation. *ECMWF Tech. Memo*., **220**, 28.

Fisher, M., Y. Trémolet, H. Auvinen, D. Tan, and P. Poli, 2011: Weak-constraint and long-window 4D-Var. *ECMWF Tech. Memo*., 655, 49.

Fisher. M and S. Gürol, 2017: Parallelization in the time dimension of four-dimensional variational data assimilation. *Q. J. R. Meteorol. So*c., 142, 1136-1147, doi:10.1002/qj.2992.

Gardiner, C.W., 1985: Handbook of Stochastic Methods for Physics, Chemistry and the Natural Sciences. Springer-Verlag, 444pp.

Gaspari, G., and S. Cohn, 1999: Construction of correlation functions in two and three dimensions. *Q. J. Roy. Meteorol. Soc*., **125**, 723–757. https://doi.org/10.1002/qj.49712555417

Giering, R. and T. Kaminski, 1998: Recipes for adjoint code construction. *ACM Trans. Math. Software*, **24**, 437-474. https://doi.org/10.1145/293686.293695

Golub, G., and C. van Loan, 1989: Matrix computations. Johns Hopkins University Press, 642 pp.

Gratton, S., D. Titley-Peloquin, P. Toint, and J. T. Ilunga, 2014: Differentiating the method of conjugate gradient. *SIAM J. Matrix Anal. & Appl*., **35**, 110–126. https://doi.org/10.1137/120889848

Gratton, S., and J. Tshimanga, 2009: An observation-space formulation of variational assimilation using a restricted preconditioned conjugate gradient algorithm. *Q. J. R. Meteorol. Soc.,* **135**, 1573–1585. https://doi.org/10.1002/qj.477

Gürol, S., A.Weaver, A.Moore, A. Piacentini, H. Arango, and S. Gratton, 2014: B-preconditioned minimization algorithms for variational data assimilation with the dual formulation. *Q. J. Roy. Meteorol. Soc*., **140**, 539–556. https://doi.org/10.1002/qj.2150

Hopson, T.M., 2014: Assessing the ensemble spread-error relationship. *Mon. Wea. Rev.*, **142**, 1125-1142. https://doi.org/10.1175/MWR-D-12-00111.1

Houtekamer, P.L., 1993: Global and local skill forecasts. *Mon. Wea. Rev.*, **121**, 1834-1846. https://doi.org/10.1175/1520-0493(1993)121<1834:GALSF>2.0.CO;2

Ide, K., P. Courtier, M. Ghil, and A. Lorenc, 1997: Unified notation for data assimilation: Operational, sequential and variational. *J. Meteorol. Soc. Japan*, **75**, 181–189. https://doi.org/10.2151/jmsj1965.75.1B_181

Klein, P., B. Hua, G. Lapeyre, X. Capet, and S. L. G. amd H. Sasaki, 2008: Upper ocean turbulence from high-resolution 3d simulations. *J. Phys. Oceanogr.*, **38**, 1748–1763. https://doi.org/10.1175/2007JPO3773.1

Lawless, A., S. Gratton, and N. Nichols, 2005: Approximate iterative methods for variational data assimilation. *J. Numer. Meth. Fl.*, **1**, 1–6. https://doi.org/10.1002/fld.851

Leith, C.E., 1974: Theoretical skill of Monte Carlo forecasts. *Mon. Wea. Rev.*, **102**, 409-356. https://doi.org/10.1175/1520-0493(1974)102<0409:TSOMCF>2.0.CO;2

Molteni, F.R., R. Buizza, T.N. Palmer and T. Petroliagis, 1996: The ECMWF ensemble system: Methodology and validation. *Q. J. Roy. Meteorol. Soc.*, **122**, 73–119. https://doi.org/10.1002/qj.49712252905

Moore, A., H. Arango, and G. Broquet, 2012: Estimates of analysis and forecast error variances derived from the adjoint of 4D-Var. *Mon. Wea. Rev.*, **140**, 3183–3203. https://doi.org/10.1175/MWR-D-11-00141.1

Moore, A.M., H.G. Arango, G. Broquet, C.A. Edwards, M. Veneziani, B. Powell. D. Foley, J. Doyle, D. Costa and P. Robinson, 2011a: The Regional Ocean Modeling system (ROMS) 4-dimensional variational data assimilation systems. Part III: Observation impact and observation sensitivity in the California current system. *Progress in Oceanography*, **91**, 74–94. https://doi.org/10.1016/j.pocean.2011.05.005

Moore, A.M., H.G. Arango, G. Broquet, B.S. Powell, J. Zavala-Garay and A.T. Weaver, 2011b: The Regional Ocean Modeling System (ROMS) 4-dimensional variational data assimilation systems: Part I system overview and formulation. *Progress in Oceanography*, **91**, 34–49. https://doi.org/10.1016/j.pocean.2011.05.004

Moore, A.M., H.G. Arango, E. DiLorenzo, B.D. Cornuelle, A.J. Miller, and D.J.Neilson, 2004: A comprehensive ocean prediction and analysis system based on the tangent linear and adjoint of a regional ocean model. *Ocean Modelling*, **7**, 227-258, doi:10.1016/j.ocemod.2003.11.001.

Ngodock, H., I. Souopgui, M. Carrier, S. Smith, J. Osborne and J. D'Addezio, 2020: An ensemble of perturbed analyses to approximate the analysis error covariance in 4dvar, *Tellus* A: *Dynamic Meteorology and Oceanography*, **72:1**, 1-12, DOI:10.1080/16000870.2020.1771069

Pedlosky, J., 1979: Geophysical Fluid Dynamics. Springer-Verlag, pp710.

Phillips, N.A., 1986: The spatial statistics of random geostrophic modes and first-guess error. *Tellus*, **38A**, 314-332. https://doi.org/10.3402/tellusa.v38i4.11721

Shchepetkin, A., and J. McWilliams, 2005: The Regional Oceanic Modeling System (ROMS): a split explicit, free-surface, topography-following-coordinate oceanic model. *Ocean Modelling*, **9**, 347–404. https://doi.org/10.1016/j.ocemod.2004.08.002

Smith, K., A. Moore, and H. Arango, 2015: Estimates of ocean forecast error covariance derived from Hessian singular vectors. *Ocean Modelling*, **89**, 104–121. https://doi.org/10.1016/j.ocemod.2015.03.003

Trémolet, Y., 2008. Computation of observation sensitivity and observation impact in incremental variational data assimilation. *Tellus* **60A**, 964–978. https://doi.org/10.1111/j.1600-0870.2008.00349.x

Umlauf, L. and H. Burchard, 2003: A generic length-scale equation for geophysical turbulence models. *J. Marine Res.*, **61**, 235-265. https://doi.org/10.1357/002224003322005087

Weaver, A., and P. Courtier, 2001: Correlation modelling on the sphere using a generalized diffusion equation. *Q. J. R. Meteorol. Soc*., **127**, 1815–1846. https://doi.org/10.1002/qj.49712757518

Weaver, A.T., C. Deltel, E. Machu, S. Ricci and N. Daget, 2005: A multivariate balance operator for variational ocean data assimilation. *Q. J. R. Meteorol. Soc*., **131**, 3605-3625. https://doi.org/10.1256/qj.05.119

Whitaker, J.S and A.F. Loughe, 1998: The relationship between ensemble spread and ensemble mean skill. *Mon. Wea. Rev.*, **126**, 3292-3302. https://doi.org/10.1175/1520-0493(1998)126<3292:TRBESA>2.0.CO;2